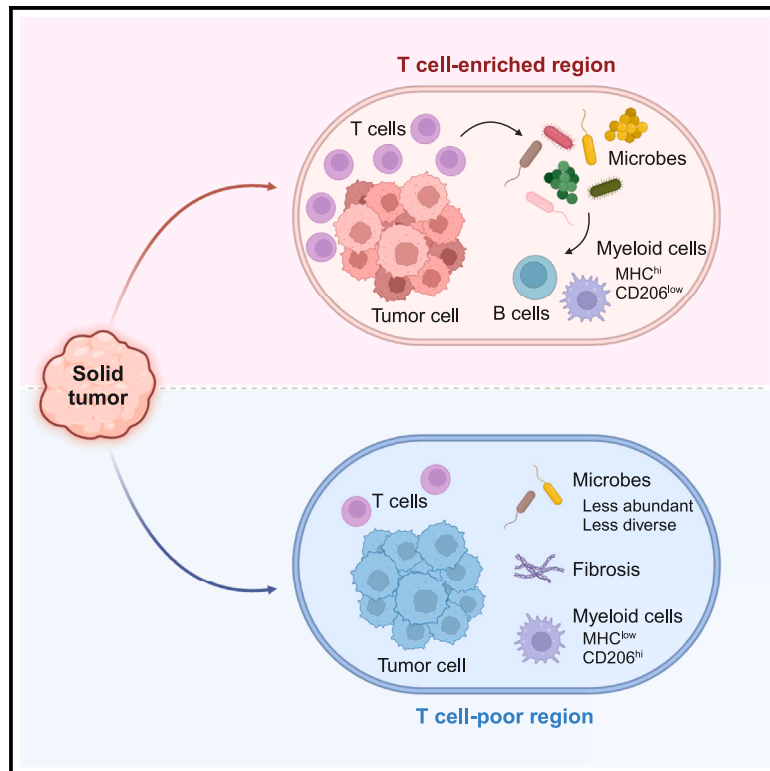**Article**

Multimodal immune phenotyping reveals microbial-T cell interactions that shape pancreatic cancer

Graphical abstract

Authors

Yan Li, Renee B. Chang,
Meredith L. Stone, ..., Won Jin Ho,
Jae W. Lee, Gregory L. Beatty

Correspondence

jlee731@jhmi.edu (J.W.L.),
gregory.beatty@pennmedicine.upenn.
edu (G.L.B.)

In brief

Li et al. show that microbial distribution in solid tumors is spatially heterogeneous and linked to T cells. Microbial-T cell interactions shape the tumor microenvironment and biology of solid tumors.

Highlights

- Microbial distribution in solid tumors is spatially heterogeneous

- Interactions between T cells and microbes shape cellular neighborhoods in cancer

- Distinct microbial-T cell interactions differentially influence tumor biology

CelPress

Article

Multimodal immune phenotyping reveals microbial-T cell interactions that shape pancreatic cancer

Yan Li,[1,2,8] Renee B. Chang,[1,2,8] Meredith L. Stone,[1,2] Devora Delman,[1,2] Kelly Markowitz,[1,2] Yuqing Xue,[1,2] Heather Coho,[1,2] Veronica M. Herrera,[1,2] Joey H. Li,[1,2] Liti Zhang,[1,2] Shaanti Choi-Bose,[1,2] Michael Giannone,[1,2] Sarah M. Shin,[3] Erin M. Coyne,[3] Alexei Hernandez,[3] Nicole E. Gross,[3] Soren Charmsaz,[3] Won Jin Ho,[3,4,5] Jae W. Lee,[3,6,7,*] and Gregory L. Beatty[1,2,9,*]

[1]Abramson Cancer Center, University of Pennsylvania, Philadelphia, PA, USA
[2]Division of Hematology-Oncology, Department of Medicine, Perelman School of Medicine, University of Pennsylvania, Philadelphia, PA, USA
[3]Sidney Kimmel Comprehensive Cancer Center, Johns Hopkins University, Baltimore, MD, USA
[4]Mass Cytometry Facility, Johns Hopkins University, Baltimore, MD, USA
[5]Convergence Institute, Johns Hopkins University, Baltimore, MD, USA
[6]Department of Pathology, Johns Hopkins University School of Medicine, Baltimore, MD, USA
[7]Sol Goldman Pancreatic Cancer Research Center, Johns Hopkins University School of Medicine, Baltimore, MD, USA
[8]These authors contributed equally
[9]Lead contact
*Correspondence: jlee731@jhmi.edu (J.W.L.), gregory.beatty@pennmedicine.upenn.edu (G.L.B.)
https://doi.org/10.1016/j.xcrm.2024.101397

SUMMARY

Microbes are an integral component of the tumor microenvironment. However, determinants of microbial presence remain ill-defined. Here, using spatial-profiling technologies, we show that bacterial and immune cell heterogeneity are spatially coupled. Mouse models of pancreatic cancer recapitulate the immune-microbial spatial coupling seen in humans. Distinct intra-tumoral niches are defined by T cells, with T cell-enriched and T cell-poor regions displaying unique bacterial communities that are associated with immunologically active and quiescent phenotypes, respectively, but are independent of the gut microbiome. Depletion of intra-tumoral bacteria slows tumor growth in T cell-poor tumors and alters the phenotype and presence of myeloid and B cells in T cell-enriched tumors but does not affect T cell infiltration. In contrast, T cell depletion disrupts the immunological state of tumors and reduces intra-tumoral bacteria. Our results establish a coupling between microbes and T cells in cancer wherein spatially defined immune-microbial communities differentially influence tumor biology.

INTRODUCTION

The tumor microenvironment (TME) is a complex ecosystem that consists of extracellular matrix and diverse populations of malignant and non-malignant cells, wherein interactions between distinct components regulate tumor progression and response to therapy. Microbes have emerged as an integral component of the TME of tumors.[1–4] Yet, the significance of the tumor microbiome remains controversial. While microbial diversity has been associated with long-term survival in patients,[4] microbes have also been suggested to mediate resistance to chemotherapies[2] and promote tumor development.[5,6] Moreover, the spatial relationship between microbes, tumor cells, and immune cells is poorly understood.

In solid tumors, diverse populations of malignant cells and immune cells engage in heterotypic interactions to form spatially heterogeneous TMEs.[7–9] Because of this shifting immune topography, a single tumor can harbor phenotypically distinct microenvironments. High-dimensional immune-based phenotyping

of human tumors has identified features in the TME that associate with survival outcomes.[10–13] Recent studies based on single-cell RNA sequencing have shown that malignant cells isolated from solid tumors exhibit an extraordinary degree of transcriptional heterogeneity.[14–18] Yet, single-cell RNA sequencing does not preserve the spatial architecture of the TME, and the mechanistic basis for the heterogeneous distribution of immune cells and microbes remains a mystery.

To preserve the spatial fidelity of the TME, we performed multiplex imaging studies to interrogate the distribution of microbes and immune cells within human pancreatic ductal adenocarcinoma (PDAC) and lung adenocarcinoma (LUAC). We used laser capture microdissection (LCM) coupled with RNA sequencing to identify distinct molecular signatures that define tumor nests in PDAC with differential microbial presences. We then used mouse models of T cell-poor and T cell-enriched tumors to understand the spatial dependency between microbes and immune cells present within the TME and their impact on tumor biology. In doing so, we established a causal relationship

between intra-tumoral microbes and T cells that was independent of the gut microbiome. Collectively, our studies reveal a non-random coupling between intra-tumoral microbes and T cells in cancer and suggest that distinct spatially defined microbial-immune communities differentially affect tumor biology, with important therapeutic implications.

RESULTS

Microbes and CD8^{+} T cells spatially co-localize within the TME

To understand the spatial distribution of microbes within the TME, we performed multiplex immunohistochemistry on human solid tumors to identify CK19^{+} cancer cells and bacteria, detected based on the expression of lipopolysaccharide (LPS; gram negative) and lipoteichoic acid (LTA; gram positive). Analyses of PDAC and LUAC revealed that the distribution of LPS was significantly variable in both tumor types (Figures 1A–1D). While a small proportion (approximately 10%) of LPS was detected within cancer cells, the majority of LPS was localized to cells within the stroma that surrounds cancer cells (Figure 1E). Similar to LPS, 16S rRNA was mostly localized to the stroma, with about 10% of 16S rRNA detected within cancer cells (Figures S1A and S1B). LPS and 16S rRNA were detected within CD68^{+} or CD15^{+} myeloid cells and cells expressing citrullinated histone H3 at even lower frequencies (Figures S1A–S1D). In addition, LTA was rarely observed in these tumor types (Figures S1E and S1F) but was detected in melanoma. These findings show that the distribution of microbes in tumors is spatially heterogeneous, dominated by gram-negative bacteria in LUAC and PDAC, and mostly limited to the stromal microenvironment.

We next studied the association between microbes and immune infiltrates in tumors by categorizing tumor regions based on the density of immune cell types surrounding CK19^{+} cancer cells (Figure 1F). The spatial heterogeneity in LPS distribution seen in PDAC was not defined by the presence of CD20^{+} B cells, CD68^{+} macrophages, or FOXP3^{+} regulatory T cells (Tregs) (Figures 1G and S1G–S1I). In contrast, LPS distribution within PDAC tumors was associated with CD8^{+} T cell infiltration (Figures 1H and 1I). Higher levels of LPS were also observed in CD8^{+} T cell-enriched regions in LUAC (Figure 1J). These findings suggested a mechanistic link between CD8^{+} T cells and microbes in tumors.

Microbial-CD8^{+} T cell enrichment identifies distinct tumor-stromal communities

We next studied the cellular and molecular contexture of tumor nests defined based on CD8^{+} T cell infiltrates. CD8^{+} T cell infiltration varied significantly across multiple human solid tumors, with inter- and intra-patient variability observed (Figure S2). Notably, the spatial distribution of CD8^{+} T cells was focal and heterogeneous in PDAC, whereas LUAC, which displayed the lowest variance in CD8^{+} T cells, contained largely uniform and homogeneous spatial distributions of CD8^{+} T cells. Based on these findings, we focused our investigations on PDAC and categorized tumor nests as CD8^{+} T cell enriched ("hot") or poor ("cold") (Figures 2A and 2B). Hot tumor nests displayed significantly higher densities of Tregs and CD68^{+} myeloid cells (Figures 2C and 2D), a higher number of CD1A^{+} dendritic cells (Figures S3A–S3C), a greater presence of components of humoral immunity (e.g., CD20^{+} B cells and immunoglobulin A [IgA][+] and IgG^{+} cells) (Figures S3B–S3E), and an increased presence of CD15^{+} myeloid cells and CD31^{+} endothelial cells in a less fibrotic milieu (Figures S3F and S3G). Cancer cells in hot and cold tumor nests also showed distinct patterns of HLA-ABC expression (Figures S3H and S3I). Notably, CK19^{+} cancer cells in hot tumor nests expressed significantly lower levels of the proliferation marker Ki-67 compared to cold tumor nests (Figures S3J and S3K), while T cells in hot tumor nests displayed higher levels of Ki-67 (Figures S3J, S3L, and S3M). PD-L1 expression was also higher in hot tumor nests (Figure S3N). Taken together, CD8^{+} T cell infiltration identified spatially distinct intra-tumoral cellular communities in PDAC.

We next developed a sequencing workflow for transcriptional analyses performed on formalin-fixed, paraffin-embedded (FFPE) tissues (Figure S4; Data S1) and then adapted this process to assess discrete regions (tumor versus stroma) within human PDAC tumors (Figure S5; Data S2). We applied this workflow to molecularly profile tumor cells and stroma in PDAC tumors, which revealed distinct biological processes associated with stroma and tumor epithelium (Figure S5). We then analyzed RNA from epithelium and stroma specifically isolated from hot and cold tumor nests using LCM (Figures 2E and S6A–S6D). Principal-component analysis of differentially expressed genes (DEGs) showed that cold and hot stroma clustered distinctly along principal component 2 (PC2), while cold and hot epithelium clustered to a lesser extent (Figure 2F). We next isolated DNA from hot and cold tumor nests and assessed for bacterial 16S rRNA. Consistent with increased LPS localization to CD8^{+} T cell-enriched tumor regions (Figure 1), hot tumor nests had a higher presence of 16S rRNA (Figure 2G). Overall, these findings show that transcriptional heterogeneity in PDAC is spatially defined and is linked to microbial and CD8^{+} T cell distribution patterns in tumors.

We next studied the biological processes that distinguish cold and hot tumor nests in human PDAC. We identified 601 DEGs between cold and hot stroma and 31 DEGs between cold and hot tumor epithelium (Data S3). Cold stroma was enriched in genes associated with epithelial-to-mesenchymal transition (EMT), MYC targets, E2F targets, myogenesis, G2M checkpoint, transforming growth factor β (TGF-β) signaling, hypoxia, and glycolysis (Figures S6E and S6F; Table S1). In contrast, hot stroma showed enrichment of genes associated with allograft rejection, interferon γ (IFNγ) response, interleukin-6 (IL-6)/JAK/STAT3 signaling, IFNα response, inflammatory response, and complement (Figures S6E and S6G; Table S1). Compared to hot tumor epithelium, cold epithelium was enriched in genes associated with E2F targets, MYC targets, G2M checkpoint, oxidative phosphorylation, DNA repair, MTORC1 signaling, and adipogenesis (Table S1). Consistent with increased microbial presence, Gene Ontology enrichment analysis of hot stroma revealed induction of genes that orchestrate host responses to bacteria (Figures 2H, 2I, and S6H). Genes involved in extracellular matrix organization including collagens and matrix metalloproteinases further distinguished cold and hot stroma
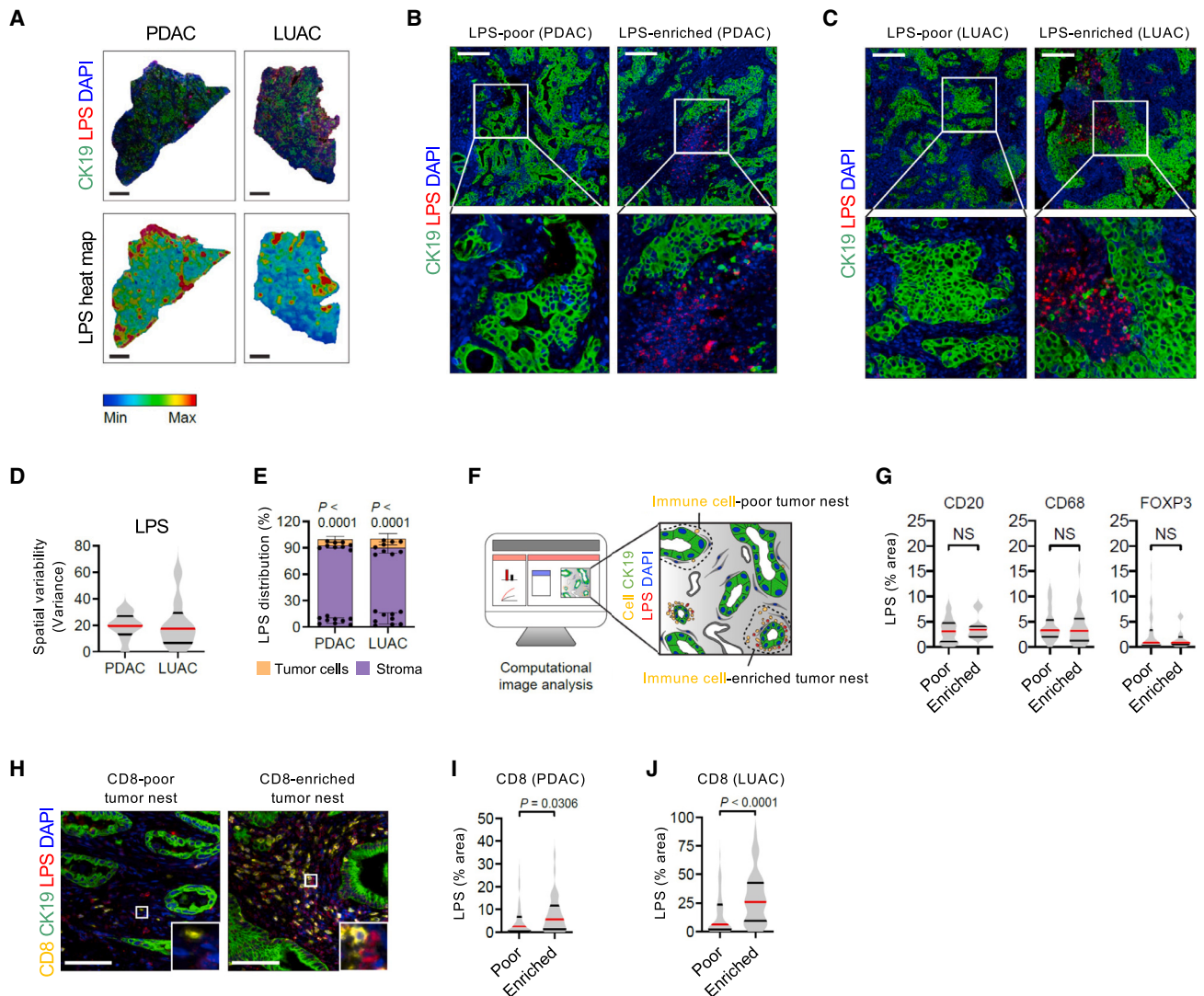
Figure 1. Microbial distribution in human solid tumors is spatially heterogeneous and coupled with CD8⁺ T cell infiltration

(A) Immunofluorescence (IF) images of CK19 (green), LPS (red), and nuclei (DAPI, blue) (top row) and heatmaps of LPS (bottom row). Scale bars, 2 mm.

(B and C) IF images of LPS-poor (left) and LPS-rich (right) regions. Scale bars, 200 μm.

(D) Spatial variance of LPS.

(E) Distribution of LPS in CK19⁺ tumor cells (yellow) and stromal cells (purple).

(F) Study design.

(G) Quantification of LPS. CD20 (n = 56 for CD20-poor and n = 11 for CD20-enriched nests pooled from 7 PDAC specimens), CD68 (n = 43 for CD68-poor and n = 28 for CD68-enriched nests pooled from 8 PDAC specimens), and FOXP3 (n = 49 for FOXP3-poor and n = 16 for FOXP3-enriched nests pooled from 9 PDAC specimens). Scale bars, 100 μm.

(H) IF images of CD8 (yellow), tumor cells (green, CK19), LPS (red), and nuclei (blue, DAPI). Scale bars, 100 μm.

(I) Quantification of LPS in PDAC tumor nests (left; n = 110 for CD8-poor nests and n = 39 for CD8-enriched nests pooled from 10 PDAC specimens).

(J) Quantification of LPS in LUAC tumor nests (right; n = 100 for CD8-poor nests and n = 50 for CD8-enriched nests pooled from 10 LUAC specimens).

For (D) and (E), n = 9 for PDAC and n = 9 for LUAC. Statistical significance was calculated using a two-tailed Mann-Whitney test (E, G, I, and J). Data are represented as violin plots (center line, median; top and bottom lines, upper and lower quartiles) and scatterplots (mean ± SD). PDAC, pancreatic ductal adenocarcinoma; LUAC, lung adenocarcinoma; NS, not significant.

(Figures S7A and S7B). Hot stroma also showed enrichment of genes involved in T and B cell chemotaxis (Figures S6H and S7C) and immune regulation (Figure S7D). Consistent with this, hot tumor nests displayed a greater presence of CD8⁺ T cells expressing markers associated with T cell exhaustion (Figures S7E–S7G). Despite expression of these molecules, hot stroma exhibited a higher degree of cytolytic activity than cold stroma (Figure S7H), which showed elevated levels of *CD276*, a molecule that has been suggested to inhibit T cell responses[19] (Figures S7I–S7K).
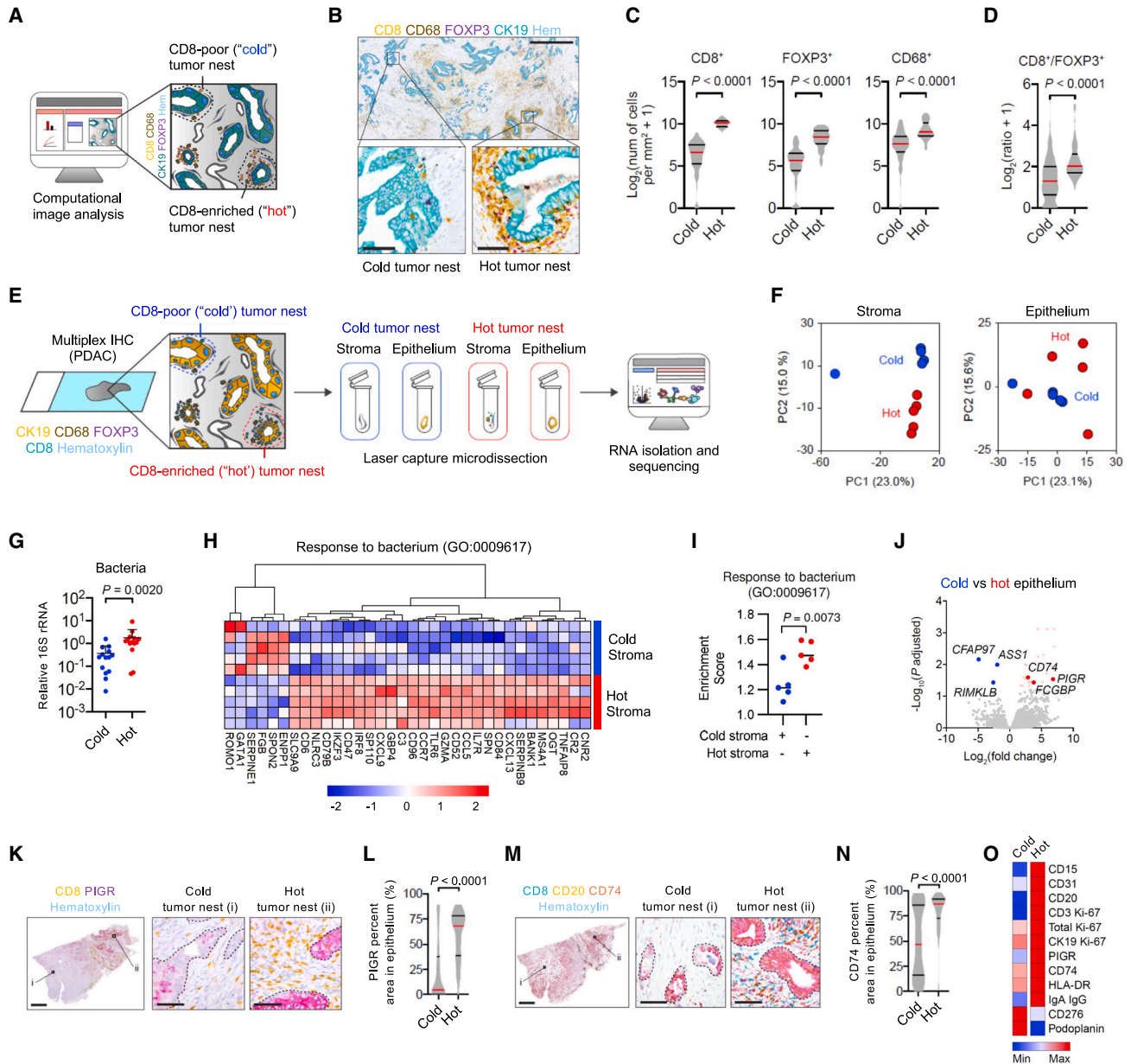
Figure 2. T cell and microbial co-localization define distinct cellular neighborhoods in human pancreatic cancer

(A) Study design for (B)–(D) (n = 185 for cold nests and n = 77 for hot nests pooled from 16 specimens).

(B) Images of CD8 (yellow), CD68 (brown), tumor epithelium (teal, CK19), FOXP3 (purple), and nuclei (blue, hematoxylin). Scale bars, 1 mm (top) and 50 μm (bottom).

(C) Quantification of CD8+ (left), FOXP3+ (middle), and CD68+ (right) cells.

(D) Ratio of CD8+ cells to FOXP3+ cells.

(E) Study design for (F) and (H)–(J).

(F) Principal-component analysis (n = 5 for hot and cold tumor nests from 1 specimen).

(G) 16S rRNA levels (n = 14 for cold and hot tumor nests from 3 patient specimens).

(H and I) Heatmap (H) and enrichment score (I) for the relative expression of genes associated with response to bacterium (GO: 0009617) in hot and cold stroma.

(J) Volcano plot of DEGs.

(K) Multiplex immunohistochemistry images of CD8 (yellow), PIGR (purple), and nuclei (blue, hematoxylin).

(L) Quantification of PIGR (n = 49 for cold nests and n = 46 for hot nests pooled from 7 specimens).

(M) Multiplex immunohistochemistry images of CD8 (teal), CD20 (yellow), CD74 (purple), and nuclei (blue, hematoxylin).

(N) Quantification of CD74 (n = 71 for cold nests and n = 45 for hot nests pooled from 10 specimens).

(legend continued on next page)

We next examined hot and cold tumor nests for potential markers of intercellular interactions that might become upregulated in cancer cells in response to the presence of microbes. Compared to cold tumor epithelium, hot tumor epithelium displayed higher levels of receptors that mediate immune responses to microbes, including PIGR and CD74 (Figures 2J–2N). Specifically, PIGR enables humoral immune responses to microbes by facilitating the transcytosis of polymeric isoforms of IgA and immune complexes,[20] and CD74 is a molecule involved in antigen presentation and has been reported to bind gut microbes, including *H. pylori*.[21] Taken together, these data show that microbial presence and immune networks, including molecules associated with acquired immune suppression, distinguish immunologically active (hot) and quiescent (cold) tumor-stromal communities in PDAC (Figure 2O).

Microbial diversity in tumors is linked to T cell infiltration

Based on our findings demonstrating a spatial coupling between microbes and T cells and enrichment of genes that orchestrate host responses to bacteria in T cell-enriched regions in human tumors, we next studied the relationship between immune cells and microbes in cancer. To do so, we utilized mouse PDAC cell lines that establish immunologically hot and cold TMEs based on T cell infiltration (Figure 3A).[16,22] As expected, PDAC cell lines injected orthotopically into syngeneic mice were distinguishable based on the presence of CD8$^+$ T cells and FOXP3$^+$ Tregs (Figure 3B). PDAC tumors also showed a spatially heterogeneous distribution of CD8$^+$ T cells (Figure 3C), similar to human PDAC. Consistent with our findings in human tumors showing that hot tumor nests harbor greater microbial presence (Figure 1), hot tumors in mice also displayed higher levels of 16S rRNA (Figure 3D). However, there was no significant difference between 16S rRNA levels in stools collected from mice bearing cold and hot tumors (Figure 3D), indicating that microbial abundance in the gastrointestinal tract is not linked to either T cell infiltration into PDAC tumors or microbial presence within tumors.

To corroborate the association between T cell infiltration and microbial presence within tumors, we analyzed five additional syngeneic PDAC cell lines[16] (Figures 3E and 3F). Here, we performed 16S rRNA quantification on tumor and stool as well as flow cytometry and immunohistochemistry to quantify the presence of multiple immune cell populations and markers of immunoregulation. As expected, principal-component analysis (PCA) and hierarchical clustering revealed two distinct patterns of immune infiltration (T cell enriched and -poor) (Figures 3E and 3F). In addition, 16S rRNA levels in tumors positively correlated with T cell infiltration (R values for correlation with CD3$^+$, CD4$^+$, and CD8$^+$ T cells were 0.49, 0.60, and 0.54, respectively) (Figure 3G). 16S rRNA levels in tumors also positively correlated with the presence of macrophages, as well as expression of CD86 and molecules involved in antigen presentation. On the other hand, 16S rRNA levels showed inverse correlations with the expression of CD206 on macrophages and tumor weight.

We next performed mRNA sequencing on cold and hot PDAC tumors isolated from syngeneic mice (Figure 3H; Data S4). PCA showed that cold and hot tumors clustered distinctly along PC1 (Figure 3I). Similar to findings in human PDAC, hot tumors in mouse PDAC showed enrichment of genes involved in immune activation (Figure S8). In contrast, cold tumors expressed genes enriched in metabolic processes, hypoxia, and cell-cycle regulation (Figure S8). Hot tumors also showed an enrichment in genes associated with response to bacterium, cell markers (*Cd20*, *Cd3e*, *Cd68*), chemokines and receptors (*Cxcl13*, *Ccl19*), and tumor epithelium markers (*Cd74*, *Pigr*) (Figures 3J–3M). Taken together, these data support a coupling between microbes and the immunological phenotype of PDAC tumors.

The tumor microbiome has been suggested to shape immune responses in PDAC.[4] Therefore, we hypothesized that the microbial compositions of hot and cold tumors would differ. Using 16S rRNA gene sequencing performed on hot and cold tumors injected orthotopically into mice, we measured the composition of bacteria in tumors (Figure 4A). As seen in human PDAC and LUAC, gram-negative bacteria dominated the tumor microbiome of hot and cold tumors (Figure 4B). We next conducted dimensional taxonomic comparisons using linear discriminant analysis (LDA) and a comparison heatmap based on operational taxonomic unit (OTU) abundance, which revealed significant differences in the predominance of bacterial communities (Figures 4C and 4D). We detected differences in bacterial communities at the various taxonomic levels (Figures 4E and S9). Hot tumors exhibited higher levels of *Arthrobacter* and *Bacillus* at the genus level and *Methylobacteriaceae* at the family level. In contrast, cold tumors were dominated by *Salirhabdus* at the genus level and *Oxalobacteraceae* at the family level.

We then measured tumor microbial α-diversity, defined as the number of species within a tumor sample, using different methodologies. α-Diversity of the tumor microbiome was significantly higher in hot tumors compared to cold tumors (Figure 4F). To examine phylogenetic relationships between bacterial communities, we used β-diversity[23,24] to generate a principal-coordinate analysis (PCoA), which revealed a distinct clustering between OTUs from hot and cold tumors (Figure 4G). In contrast, gut microbiota in stool showed a significant reduction in microbial α-diversity between tumor-free and tumor-bearing mice, with no difference between mice with hot tumors compared to cold tumors (Figure 4H). Further, gut microbial β-diversity distinguished tumor-free and tumor-bearing mice but was similar between mice with hot tumors and cold tumors (Figure 4I). Thus, the abundance, diversity, and composition of the gut microbiota are altered by PDAC but are not necessarily determinants of T cell infiltration into tumors. In addition, these data suggest that the gut and tumor microbiomes in PDAC are uncoupled, with distinct intra-tumoral microbial communities defined by the presence or absence of infiltrating T cells.

(O) Summary of cell markers and proteins.

For (K) and (M), scale bars, 2 mm (left) and 50 μm (right), and dashed lines indicate tumor epithelium. Statistical significance was calculated using a two-tailed Mann-Whitney test. Data are represented as violin plots (center line, median; top and bottom lines, upper and lower quartiles) and scatterplots (mean + SD or mean). PDAC, pancreatic ductal adenocarcinoma.
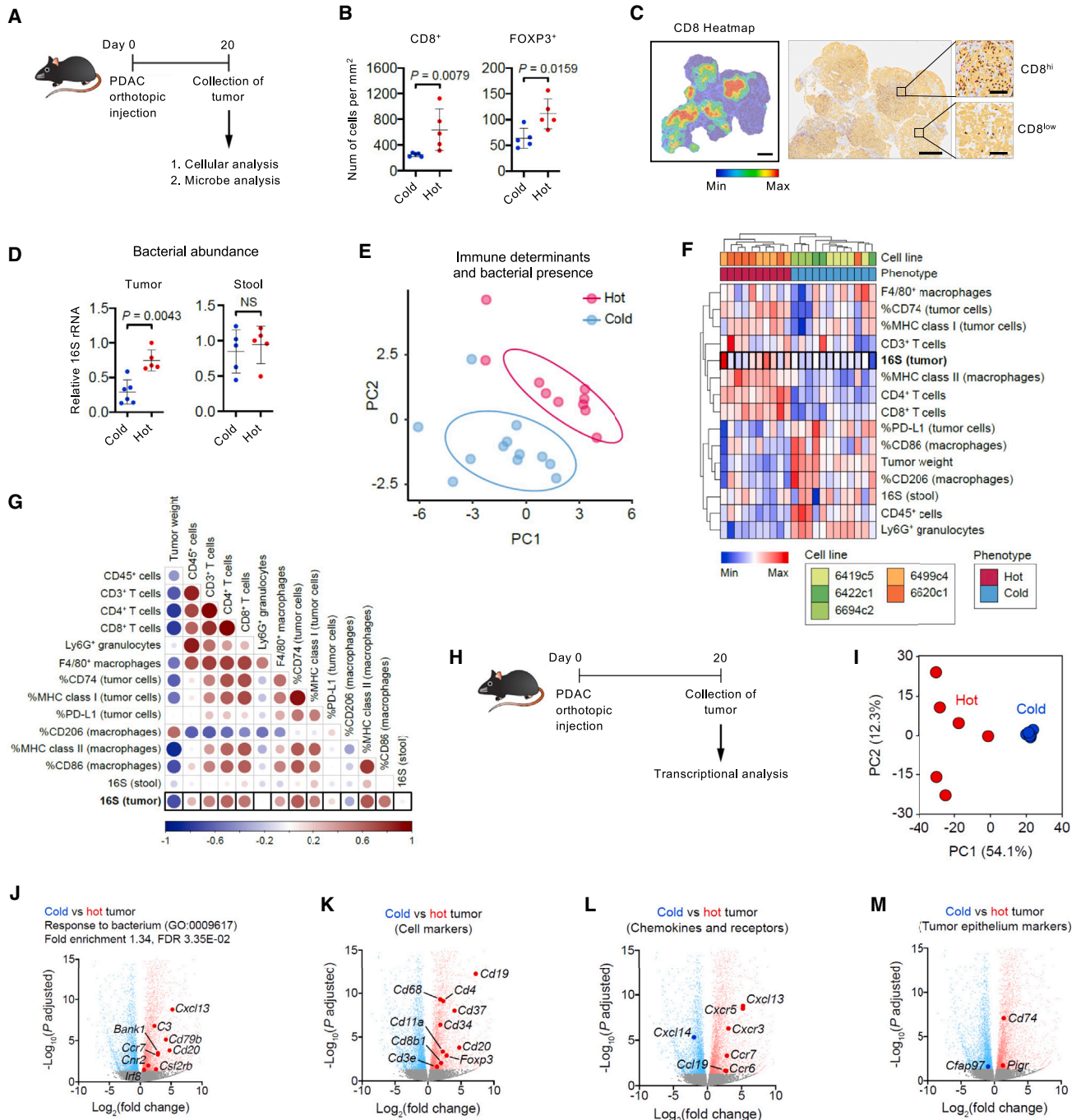
Figure 3. The tumor microbiome is linked to T cell infiltration in murine PDAC

(A) Study design for (B)–(D) (n = 5–6 for mice orthotopically injected with cold [69] and hot [2838c3] PDAC cells).

(B) Quantification of intra-tumoral CD8+ and FOXP3+ T cells.

(C) Representative heatmap (left) of CD8+ T cells in murine hot PDAC tumor and corresponding multiplex immunohistochemistry images (right) of CD8 (brown), FOXP3 (purple), tumor cells (yellow, CK19), and nuclei (blue, hematoxylin). Scale bars, 1 mm and 100 μm (insets).

(D) 16S rRNA levels in cold and hot orthotopic tumors (left) and stool (right).

(E–G) Mice (n = 3–5 per group) were orthotopically injected with cold (n = 3) and hot (n = 2) PDAC cell lines. Principal-component analysis (E) of immune and bacterial determinants displayed in heatmap (F). (G) Correlation plot.

(H) Study design for (I)–(M) (n = 6 for mice orthotopically injected with cold [69] and hot [2838c3] tumor cells).

(legend continued on next page)

Tumor microbiome communities are instructed by T cells and differentially impact tumor biology

To interrogate the causal relationship between intra-tumoral T cells and microbes, mice were orthotopically injected with PDAC cells that form cold and hot tumors and then treated with a triple-antibiotic cocktail consisting of metronidazole, ceftriaxone, and vancomycin (Figure 5A). Antibiotic treatment effectively depleted bacteria in hot tumors and stool (Figure 5B) but did not impact CD8$^+$ T cell or Treg infiltration into the tumors (Figures 5C and 5D). In cold tumors, bacterial abundance was significantly less than in hot tumors (Figure 5B), was not further decreased by antibiotic treatment (Figure 5E), and did not impact CD8$^+$ T cell or Treg presence (Figure 5F). Antibiotic treatment differentially altered the transcriptional profile of cold and hot tumors (Figure 5G; Data S5). Genes downregulated in hot tumors with antibiotics were associated with pancreatic secretion, inflammatory response, and innate immunity, whereas genes downregulated in cold tumors were associated with pancreatic secretion, MAPK signaling pathway, and positive regulation of cell proliferation (Figures 5H and S10). Tumor growth was also differentially impacted by antibiotics, as seen by a reduction in tumor weights for cold tumors but not hot tumors (Figures 5I and 5J). We next examined the impact of antibiotics on the phenotype and presence of myeloid cells and B cells, which were found to be differentially associated with cold and hot tumors in mice (Figure 3) and humans (Figure 2 and S3). Consistent with the immunomodulatory potential of microbes, antibiotic treatment decreased the density of intra-tumoral CD19$^+$ B cells in hot tumors (Figure 5K). Further, antibiotics decreased the expression levels of major histocompatibility complex (MHC) class II molecules on intra-tumoral macrophages, with a concomitant increase in the immunosuppressive marker CD206 (Figures 5L and 5M). Together, these data indicate that T cell surveillance in cancer can occur independent of intra-tumoral and gut microbiota but, nonetheless, implicate a role for intra-tumoral bacteria in shaping the cellular contexture of the TME.

We next considered the possibility that microbial presence in tumors is dependent on T cells. To test this hypothesis, mice with or without T cell depletion were orthotopically injected with PDAC cells that form hot tumors (Figures 6A, S11A, and S11B). As expected, genes associated with T cells as well as myeloid cell populations were decreased in hot tumors depleted of T cells (Figure S11C; Data S5). PCA revealed that cold tumors and hot tumors with and without T cells each clustered distinctly (Figure 6B). These findings indicated a significant role for T cells in defining the transcriptional profile of PDAC tumors but also suggested that other determinants contribute to transcriptional differences seen between cold and hot tumors. Consistent with a role for T cells in regulating the microbial response to PDAC, Gene Ontology enrichment analysis showed an increase in genes that orchestrate host responses to bacteria in hot

compared to cold tumors, with a significant decrease in hot tumors when T cells were depleted (Figure 6C). Further, microbial-associated genes *Pigr* and *Cd74*, which are increased in hot tumor cells in human PDAC (Figure 2), were also enriched in hot tumors compared to hot tumors with T cell depletion (Figure S11D). T cell depleted tumors were greater in weight (Figure 6D), and 16S rRNA levels were decreased in hot tumors in the absence of T cells (Figure 6E). In contrast, no effect was seen on 16S rRNA levels detected in stool (Figure 6F). These findings indicate that microbial-T cell coupling in PDA tumors is directed by T cells rather than microbes.

Finally, we studied the impact of T cells on the TME and microbial composition in tumors. T cell presence in hot tumors was associated with genes enriched in antigen processing and presentation of endogenous peptide antigen and cytokine production (Figure S12). However, T cell presence in tumors was also associated with genes enriched in response to LPS, B cell activation, and the Toll-like receptor signaling pathway. Consistent with this, T cell depletion reduced CD19$^+$ B cell infiltration into hot tumors like that seen with antibiotic treatment (Figures S11E and S11F). In addition, T cell depletion caused a shift in myeloid cell phenotype, with a decrease in MHC class II on intra-tumoral macrophages and a concomitant increase in the immunosuppressive marker CD206 (Figures S11G–S11I).

To deepen the characterization of immune cells and to study their relationship to microbial presence in more detail, we next performed image mass cytometry (IMC) and compared the cellular composition of hot tumors and hot tumors that were depleted of T cells (Figure S13A). T cell depletion decreased the density of all T cell subsets (Figure S13B). Consistent with flow cytometric results (Figures S11G–S11I), T cell depletion also decreased the density of myeloid cells expressing MHC class II and CD86 (myeloid cell subset 2), whereas the density of myeloid cells that expressed CD206 (myeloid cell subsets 3–6) increased in response to T cell depletion (Figures S13B and S13C). Consistently, T cell depletion also decreased the presence of LPS and 16S rRNA within the tumor (Figures S13C and S13D). In contrast, T cell depletion increased the number of endothelial cells and vessel patency (Figures S13B, S13C, S13E, and S13F). These findings support a coupling between T cells and microbes in shaping the contexture of the TME (Figure S13G).

We next performed dimensional taxonomic comparisons on hot tumors with and without T cells, which revealed similar bacterial communities (Figures 6G and S14). Consistent with this, tumor microbial β-diversity was also similar between hot tumors with and without T cells (Figure 6H). In contrast, tumor microbial α-diversity was significantly decreased in hot tumors in the absence of T cells (Figure 6I). These findings indicate that T cells direct microbial accumulation in tumors but do not influence the composition of the tumor microbiome. Taken together, our findings establish a causal link between T cells and microbes

---

(I) Principal-component analysis.

(J–M) Volcano plots.

Data are representative of three independent experiments (B–D) or two independent experiments (H–M). Statistical significance was calculated using a two-tailed Mann-Whitney test (B and D). Data are represented as scatterplots (mean ± SD). FDR, false discovery rate; NS, not significant.
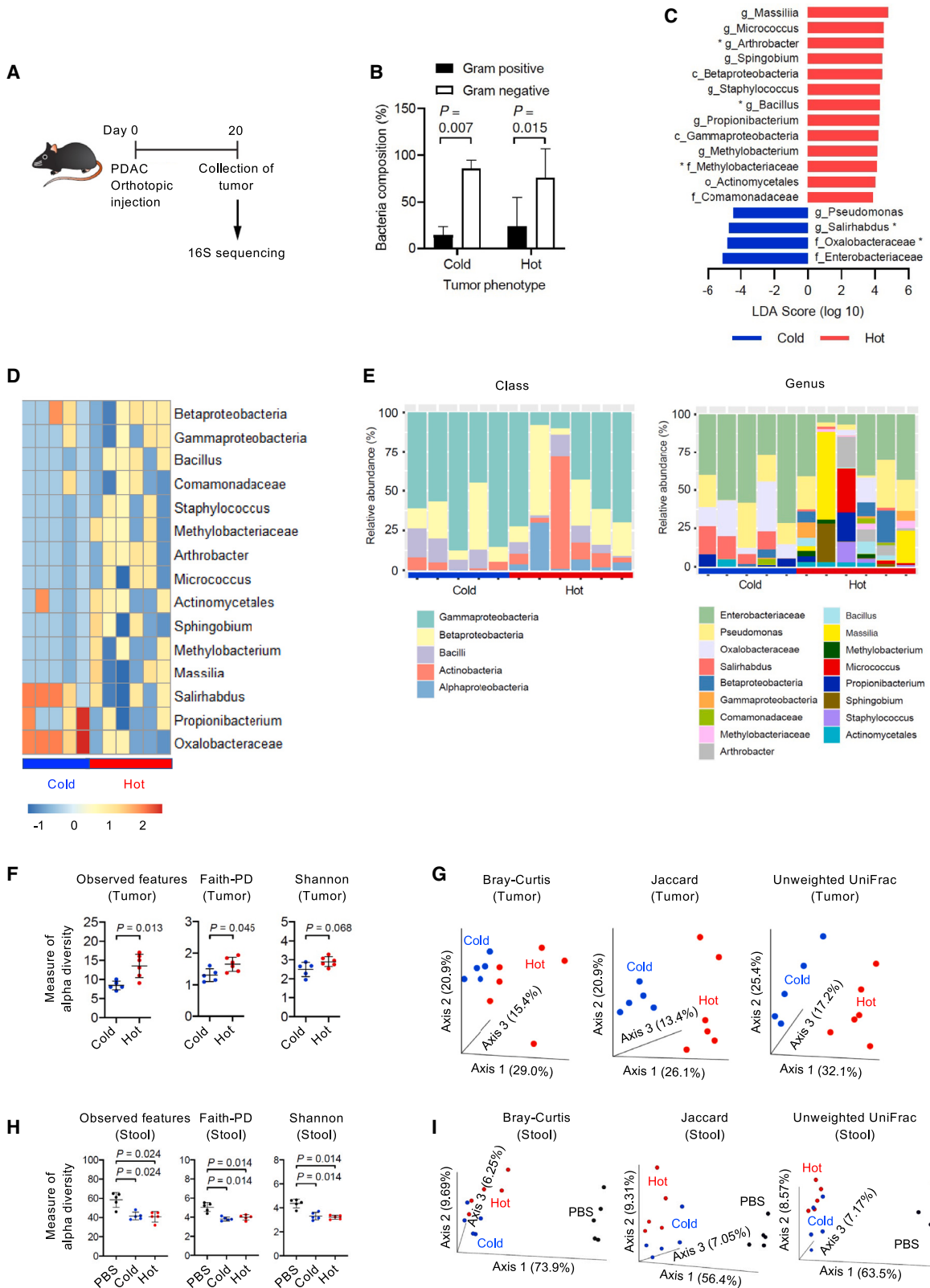
(legend on next page)

in cancer and show that T cells coordinate this relationship and, in doing so, define spatially and molecularly distinct cellular communities within tumors.

DISCUSSION

In this study, we incorporated spatial-profiling technologies along with clinically relevant mouse models to interrogate the causal relationship between microbes and immune cells in defining spatial heterogeneity in cancer. We show that a non-random coupling between microbial and immune communities within human and mouse pancreatic tumors shapes the biology of distinct intra-tumoral niches. Microbial-T cell coupling in tumors was coordinated by T cells rather than by intra-tumoral microbes. Further, this relationship was independent of the gut microbiome, which, although altered by tumor development, was not a determinant of T cell infiltration into tumors or intra-tumoral microbial diversity and composition.

Recent studies implicate the gut and tumor microbiomes as integral components of the immunobiology of solid tumors.[1–4,6] In human PDAC, higher diversity of bacteria within tumors associates with T cell infiltration and correlates strongly with increased long-term survival.[4] While cancer-cell-intrinsic factors, including CXCL1,[16] G-CSF/GM-CSF,[25,26] EPHA2,[27] USP22,[28] and β-catenin,[29] have been shown to suppress anti-tumor immunity, the precise immunoregulatory impact of gut and intra-tumoral microbes on immunosurveillance in PDAC has remained unclear. Fecal microbiota transplants have been used as one approach to examine the role of the gut microbiota in regulating tumor biology.[4,30–35] These studies have revealed the potential of fecal transplantation as a therapeutic intervention capable of triggering immune activation against tumors. These studies also raised the hypothesis that the gut microbiome is a determinant of immune biology. Consistent with this, some microbes found within tumor specimens appear to share a gut origin, suggesting the possibility for translocation of bacteria from the gut to the tumor.[36]

In contrast to previous studies, we used syngeneic tumor models of PDAC that naturally establish immunologically active or quiescent TMEs and intra-tumoral microbiome to investigate a link between microbes and the immunobiology of PDAC. Consistent with prior work, we found that the gut microbiome of tumor-bearing mice was distinct from tumor-free mice. However, the gut microbiome of mice with T cell-enriched tumors was indistinguishable from the gut microbiome of mice with T cell-poor tumors, whereas the microbial composition and

abundance of T cell-enriched and -poor tumors were significantly different. This finding is consistent with the co-existence of T cell-enriched and -poor niches, which corresponded to microbe-enriched and -poor niches, respectively, in pancreatic tumors and supports a role for cancer-cell-intrinsic determinants rather than the gut microbiome in defining tumor-immune-microbial communities. We also found that hot tumor nests in human PDAC had higher microbial abundance compared to cold tumor nests. However, we were not able to perform 16S rRNA metagenomic sequencing to assess the microbial composition due to the insufficient amounts of bacterial DNA that we were able to collect from tumor nests isolated using LCM.

Cancer cells co-exist with many microenvironmental components, including a variety of tissue-associated cells, immune cells, extracellular matrix, soluble factors, and microbes. These cancer-cell-extrinsic determinants influence tumor evolution and shape treatment outcomes. The heterogeneous distribution of these factors within tumors has complicated studies to understand reciprocal interactions between elements of the TME. For this reason, we studied resected cancer, rather than biopsies, to allow for assessment of this biology. Our data show that microbes and T cells co-localize in tumors and that this interdependence is coordinated by T cells, which enhance intra-tumoral microbial presence. We considered the possibility that T cells may promote increased vascularity in tumors, which in turn facilitates the accumulation of microbes. However, tumors that were depleted of T cells showed enrichment in genes associated with angiogenesis (Figure S12) and a greater presence of patent blood vessels (Figure S13). This finding suggests that changes in the vasculature may in turn alter microbial abundance through changes in the delivery of nutrients and metabolites. In addition, T cell depletion and antibiotic treatment increased the presence of CD206+ myeloid cells. As a C-type lectin that is predominantly expressed by myeloid cells, CD206 (mannose receptor) recognizes a range of microbes, including bacteria, fungi, and viruses.[37] Thus, CD206+ myeloid cells that become enriched in tumors in response to T cell depletion and/or antibiotic treatment may render tumors less susceptible to microbial growth.

Prior work also suggests that intra-tumoral bacteria may be mostly intracellular and present in both cancer and immune cells.[3,38,39] Consistent with this, our data show that gram-negative bacteria, detected using LPS and 16S rRNA, are found within tumor cells and stromal cell populations, including CD68+ macrophages. CD8+ T cells were also located in close proximity to LPS. Thus, it is possible that T cells support microbial presence in tumors by actively transporting bacteria and by recruiting

Figure 4. Intra-tumoral microbial composition and diversity distinguish T cell-enriched and T cell-poor tumors
(A) Study design for (B)–(I) (n = 5, 5, and 6 for mice orthotopically injection with PBS, cold [69], and hot [2838c3] PDAC cells, respectively).
(B) Percentage of composition of gram-negative and gram-positive bacteria in cold and hot tumors.
(C) Linear discriminant analysis.
(D) Heatmap of bacterial features at the genus level.
(E) Taxonomic compositions at the class and genus levels.
(F) α-Diversity in tumor.
(G) Principal-coordinate analysis (PCoA) of tumor.
(H) α-Diversity in stool.
(I) PCoA of stool.
Data are representative of two independent experiments (B–I). Statistical significance was calculated using a two-tailed Mann-Whitney test (B and F) and a Kruskal-Wallis test (C and H). Data are represented as scatterplots (mean ± SD).
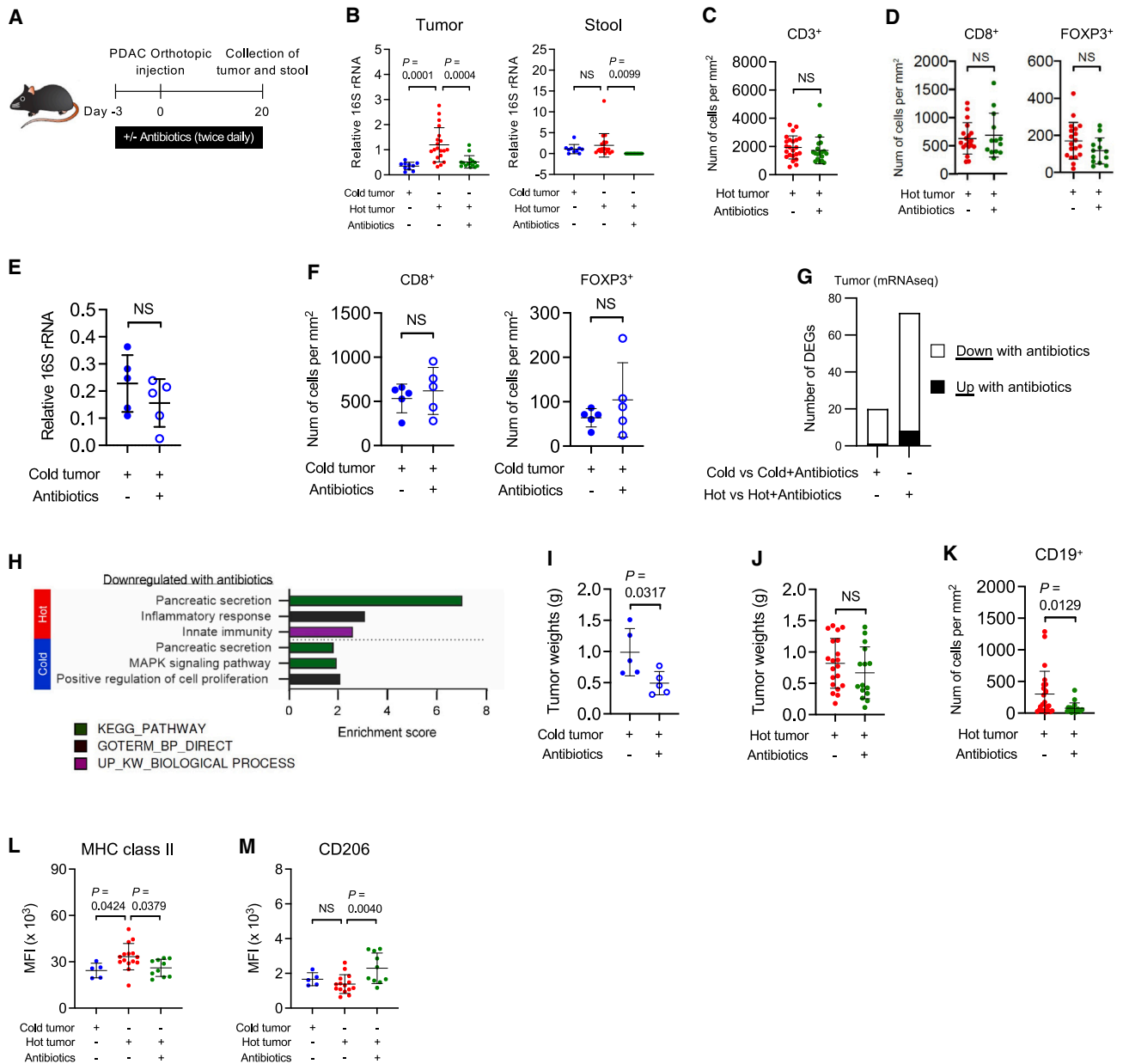
Figure 5. T cell infiltration into tumors occurs independent of the gut and tumor microbiome

(A) Study design for (B)–(K).

(B) 16S rRNA levels in tumor and stool from mice orthotopically injected with cold (69) tumor cells (n = 10) or hot (2838c3) tumor cells and treated with (n = 15) and without (n = 20) antibiotics.

(C and D) Quantification of CD3⁺ (C) and CD8⁺ and FOXP3⁺ (D) T cells from hot tumors of mice treated with (n = 19) or without (n = 13) antibiotics.

(E) 16S rRNA levels in tumor from mice orthotopically injected with cold (69) tumor cells and treated with (n = 5) and without (n = 5) antibiotics.

(F) Quantification of CD8⁺ and FOXP3⁺ T cells from cold tumors of mice treated with (n = 5) and without (n = 5) antibiotics.

(G) Number of DEGs.

(H) Bar graph displaying overrepresentation analysis of DEGs in indicated gene sets.

(I and J) Tumor weights at day 20.

(K) Quantification of intra-tumoral CD19⁺ cells.

(L and M) Mean fluorescence intensity (MFI) of MHC class II (L) and CD206 (M) on CD11b⁺ F4/80⁺ intra-tumoral macrophages.

Data were pooled from two to three experiments (B–D and J–M) or are representative of two independent experiments (E–I). Statistical significance was calculated using one-way ANOVA with Dunnett's test (B, L, and M) and a two-tailed Mann-Whitney test (C–F and I–K). Data are represented as scatterplots (mean ± SD). NS, not significant.
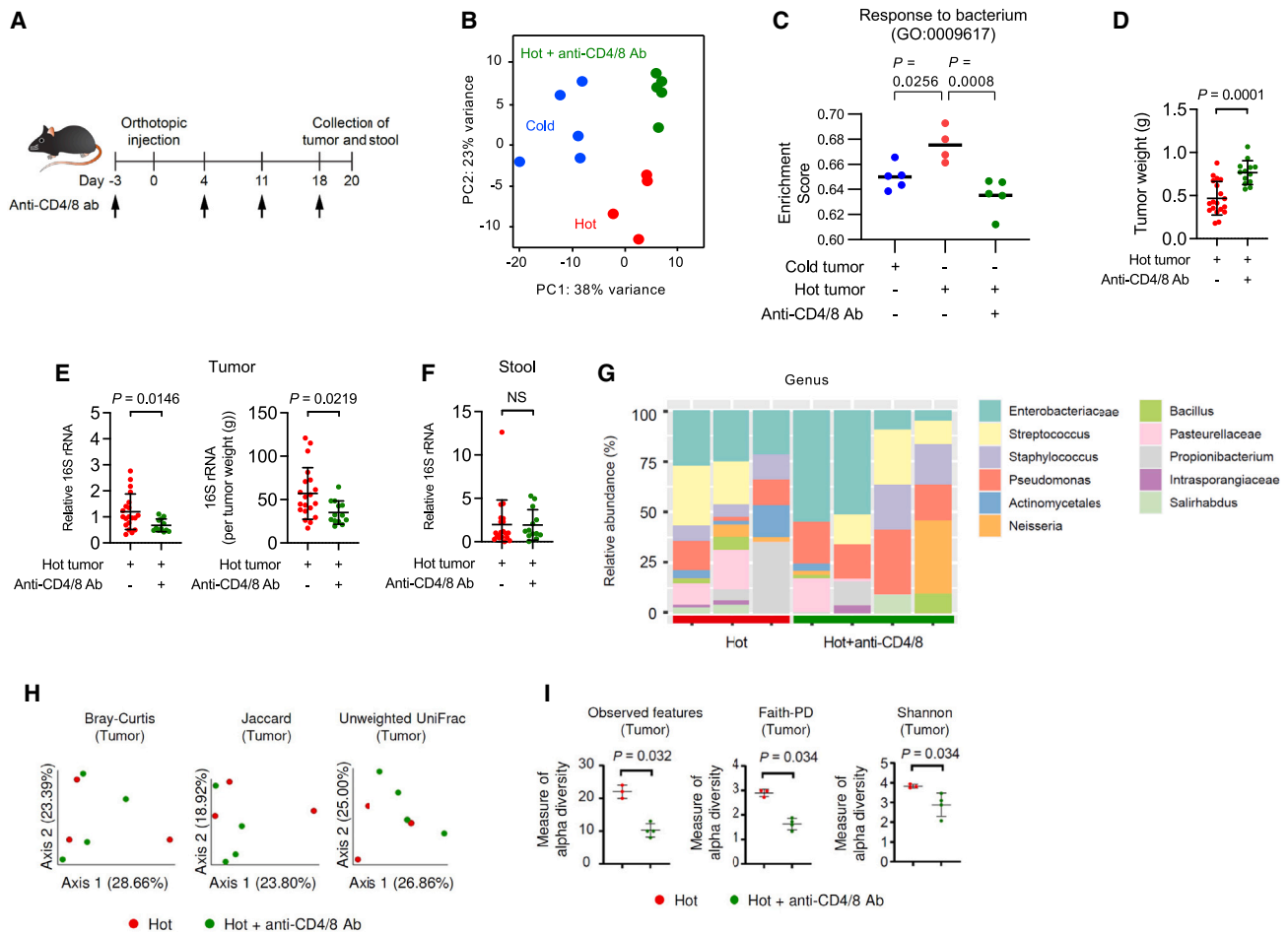
Figure 6. T cells promote the accumulation of intra-tumoral microbes without affecting microbial composition
(A) Study design for (B)–(H).
(B) Principal-component analysis of mRNA sequencing data.
(C) Enrichment score for the relative expression of genes associated with response to bacterium (GO: 0009617).
(D–F) Tumor weights at day 20 (D) and 16S rRNA levels in tumor (E) and stool (F) from mice orthotopically injected with cold (69) tumor cells (n = 10) or hot (2838c3) tumor cells and treated with (n = 20) or without (n = 12–13) anti-CD4/CD8 antibodies.
(G) Taxonomic compositions at the genus level.
(H) PCoA of tumor.
(I) α-Diversity in tumor.
Data were pooled from two experiments (D–F). Statistical significance calculated using a two-tailed Mann-Whitney test. Data are represented as scatterplots (mean ± SD). NS, not significant.

other cells that harbor intracellular bacteria. While not addressed in our present study, future studies that investigate the origin of intra-tumoral microbes and their interactions with immune cells at the site of origin may reveal cellular mediators of microbial entry into primary as well as metastatic tumors. Our data also show that T cells are not determinants of the microbial composition in tumors, suggesting that other factors, such as extracellular matrix composition or metabolites within the tumor stroma, may select for distinct microbes.

Our study provides evidence that distinct microbial communities can differentially influence tumor biology. Using mouse models of PDAC, we found that microbial composition in tumors differed between T cell-poor and -enriched tumors. Microbes in

T cell-poor tumors supported tumor growth, whereas microbes in T cell-enriched tumors facilitated B cell infiltration and the upregulation of immunostimulatory molecules on intra-tumoral macrophages. We hypothesize that this dichotomy in microbial influence on tumor biology reflects the distinct composition of intra-tumoral microbes. This may explain the paradoxical findings of microbes seen in preclinical and translational studies wherein microbes can contribute to chemotherapeutic resistance and tumor progression[2,5,6] but can also trigger anti-tumor immunity.[4,30–35] In addition, it is possible that the relationship between microbes and the phenotype of tumor-immune communities may differ based on cancer type and anatomic location of disease. In this regard, we found that gram-positive bacteria

were common to melanoma lesions but undetectable by immunohistochemistry in LUAC and PDAC. Consistent with this, the microbiome composition can differ by cancer type.[3]

We studied murine models of PDAC that mirror the T cell-enriched and T cell-poor TMEs seen in human disease. Notably, these murine models are known to respond differently to immunotherapy.[16] Given the remarkable spatial heterogeneity defined by T cells and microbes in human cancer, we propose that discrete regions of tumors may also respond differently to therapeutic interventions. To this end, it remains unclear whether changes in the TME produced by chemotherapy or immunotherapy remodel microbial communities in tumors and whether enrichment in distinct microbes in the setting of treatment influences outcomes. Our data also showed that T cell-enriched and -poor tumors responded differently to antibiotic treatment. While antibiotics inhibited the growth of T cell-poor tumors, the growth of T cell-enriched tumors was not affected. Further, myeloid cells in T cell-enriched tumors acquired an immunosuppressive phenotype in response to antibiotic treatment, suggesting that antibiotic treatment may shape how discrete regions of tumors may respond to chemotherapy or immunotherapy. In addition, our studies do not address other components of the microbiome, including the contribution of fungal components, which may perturb the TME in distinct ways.[40] Regardless, this work shows collectively that the spatial distribution of intra-tumoral microbiota in human and mouse cancer is non-random, not necessarily dependent on the gut microbiome, and linked to discrete tumor-immune cellular communities with differential activity on cancer cells.

Limitations of the study

While our study demonstrates that T cells are necessary for the accumulation of intra-tumoral microbes, our data do not define the precise molecular mechanisms by which T cells regulate the presence of microbes within tumors. To this end, it is possible that multiple factors converge to establish a microenvironment that is conducive for distinct microbes. For example, while our data show the importance of T cells in coordinating this microenvironment, it remains unclear whether T cells are directly and solely responsible for microbial accumulation within tumors or if other cells and factors also contribute. Finally, our study focused on the spatial coupling between immune cells and intra-tumoral bacteria. Future studies will need to consider other components of the tumor microbiome, including fungal species. This knowledge may further inform mechanisms by which immune cells shape the distribution of distinct microbes in tumors.

STAR★METHODS

Detailed methods are provided in the online version of this paper and include the following:

- KEY RESOURCES TABLE
- RESOURCE AVAILABILITY
  - Lead contact
  - Materials availability
  - Data and code availability
- EXPERIMENTAL MODEL AND STUDY PARTICIPANT DETAILS
  - Human samples
  - Cell lines
  - *In vivo* studies
- METHOD DETAILS
  - Microscopic analysis
  - Immunohistochemistry image analysis
  - Immunofluorescence image analysis
  - RNA and laser capture microdissection (LCM)
  - RNA sequencing and data analysis
  - Flow cytometry
  - 16S rRNA gene quantification
  - 16S rRNA metagenomic sequencing and analysis
  - Image mass cytometry (IMC)
  - Correlation analysis
- QUANTIFICATION AND STATISTICAL ANALYSIS

AUTHOR CONTRIBUTIONS

Experiments and data analysis were performed by Y.L., R.B.C., M.L.S., D.D., K.M., Y.X., H.C., V.M.H., J.H.L., L.Z., S.C.-B., M.G., S.M.S., E.M.C., A.H., N.E.G., S.C., W.J.H., J.W.L., and G.L.B; immunofluorescence and immunohistochemistry by Y.L., R.B.C., D.D., K.M., Y.X., J.H.L., S.C.-B., and J.W.L.; RNA *in situ* hybridization by Y.L., R.B.C., Y.X., J.H.L., and J.W.L.; computational image analysis by R.B.C., Y.X., and J.H.L.; LCM and isolation of RNA by Y.L.; RNA sequencing and data analysis by Y.L. and J.W.L.; isolation and identification of bacteria from mouse tumors by Y.L.; 16S rRNA quantitative PCR and 16S rRNA metagenomic sequencing and analysis by Y.L.; compilation of patient characteristics by D.D., K.M., R.B.C., and M.G.; animal studies by Y.L., M.L.S., H.C., and V.M.H.; flow cytometry by V.M.H. and Y.L.; IMC by S.M.S., E.M.C., A.H., N.E.G., S.C., W.J.H., and J.W.L.; Y.L., R.B.C., M.L.S., J.W.L., and G.L.B. designed the study; and Y.L., R.B.C., J.W.L., and G.L.B. prepared and wrote the manuscript.

DECLARATION OF INTERESTS

W.J.H. reports royalties from Rodeo/Amgen; grants from Sanofi, NeoTX, and Circle Pharma; and prior consulting fees from Exelixis. G.L.B. reports prior

REFERENCES

1. Fu, A., Yao, B., Dong, T., Chen, Y., Yao, J., Liu, Y., Li, H., Bai, H., Liu, X., Zhang, Y., et al. (2022). Tumor-resident intracellular microbiota promotes metastatic colonization in breast cancer. Cell *185*, 1356–1372.e26.

2. Geller, L.T., Barzily-Rokni, M., Danino, T., Jonas, O.H., Shental, N., Nejman, D., Gavert, N., Zwang, Y., Cooper, Z.A., Shee, K., et al. (2017). Potential role of intratumor bacteria in mediating tumor resistance to the chemotherapeutic drug gemcitabine. Science *357*, 1156–1160.

3. Nejman, D., Livyatan, I., Fuks, G., Gavert, N., Zwang, Y., Geller, L.T., Rotter-Maskowitz, A., Weiser, R., Mallel, G., Gigi, E., et al. (2020). The human tumor microbiome is composed of tumor type-specific intracellular bacteria. Science *368*, 973–980.

4. Riquelme, E., Zhang, Y., Zhang, L., Montiel, M., Zoltan, M., Dong, W., Quesada, P., Sahin, I., Chandra, V., San Lucas, A., et al. (2019). Tumor Microbiome Diversity and Composition Influence Pancreatic Cancer Outcomes. Cell *178*, 795–806.e12.

5. Jin, C., Lagoudas, G.K., Zhao, C., Bullman, S., Bhutkar, A., Hu, B., Ameh, S., Sandel, D., Liang, X.S., Mazzilli, S., et al. (2019). Commensal microbiota promote lung cancer development via γδ t cells. Cell *176*, 998–1013.e16.

6. Pushalkar, S., Hundeyin, M., Daley, D., Zambirinis, C.P., Kurz, E., Mishra, A., Mohan, N., Aykut, B., Usyk, M., Torres, L.E., et al. (2018). The pancreatic cancer microbiome promotes oncogenesis by induction of innate and adaptive immune suppression. Cancer Disc *8*, 403–416.

7. Azizi, E., Carr, A.J., Plitas, G., Cornish, A.E., Konopacki, C., Prabhakaran, S., Nainys, J., Wu, K., Kiseliovas, V., Setty, M., et al. (2018). Single-cell map of diverse immune phenotypes in the breast tumor microenvironment. Cell *174*, 1293–1308.e36.

8. Jiménez-Sánchez, A., Memon, D., Pourpe, S., Veeraraghavan, H., Li, Y., Vargas, H.A., Gill, M.B., Park, K.J., Zivanovic, O., Konner, J., et al. (2017). Heterogeneous tumor-immune microenvironments among differentially growing metastases in an ovarian cancer patient. Cell *170*, 927–938.e20.

9. Moncada, R., Barkley, D., Wagner, F., Chiodin, M., Devlin, J.C., Baron, M., Hajdu, C.H., Simeone, D.M., and Yanai, I. (2020). Integrating microarray-based spatial transcriptomics and single-cell RNA-seq reveals tissue architecture in pancreatic ductal adenocarcinomas. Nat. Biotechnol. *38*, 333–342.

10. Carstens, J.L., Correa de Sampaio, P., Yang, D., Barua, S., Wang, H., Rao, A., Allison, J.P., LeBleu, V.S., and Kalluri, R. (2017). Spatial computation of intratumoral T cells correlates with survival of patients with pancreatic cancer. Nat. Commun. *8*, 15095.

11. Chevrier, S., Levine, J.H., Zanotelli, V.R.T., Silina, K., Schulz, D., Bacac, M., Ries, C.H., Ailles, L., Jewett, M.A.S., Moch, H., et al. (2017). An immune atlas of clear cell renal cell carcinoma. Cell *169*, 736–749.e18.

12. Liudahl, S.M., Betts, C.B., Sivagnanam, S., Morales-Oyarvide, V., da Silva, A., Yuan, C., Hwang, S., Grossblatt-Wait, A., Leis, K.R., Larson, W., et al. (2021). Leukocyte heterogeneity in pancreatic ductal adenocarcinoma: phenotypic and spatial features associated with clinical outcome. Cancer Disc *11*, 2014–2031.

13. Tsujikawa, T., Kumar, S., Borkar, R.N., Azimi, V., Thibault, G., Chang, Y.H., Balter, A., Kawashima, R., Choe, G., Sauer, D., et al. (2017). Quantitative multiplex immunohistochemistry reveals myeloid-inflamed tumor-immune complexity associated with poor prognosis. Cell Rep. *19*, 203–217.

14. Chung, W., Eum, H.H., Lee, H.O., Lee, K.M., Lee, H.B., Kim, K.T., Ryu, H.S., Kim, S., Lee, J.E., Park, Y.H., et al. (2017). Single-cell RNA-seq enables comprehensive tumour and immune cell profiling in primary breast cancer. Nat. Commun. *8*, 15081.

15. Lawson, D.A., Kessenbrock, K., Davis, R.T., Pervolarakis, N., and Werb, Z. (2018). Tumour heterogeneity and metastasis at single-cell resolution. Nat. Cell Biol. *20*, 1349–1360.

16. Li, J., Byrne, K.T., Yan, F., Yamazoe, T., Chen, Z., Baslan, T., Richman, L.P., Lin, J.H., Sun, Y.H., Rech, A.J., et al. (2018). Tumor cell-intrinsic factors underlie heterogeneity of immune cell infiltration and response to immunotherapy. Immunity *49*, 178–193.e7.

17. Puram, S.V., Tirosh, I., Parikh, A.S., Patel, A.P., Yizhak, K., Gillespie, S., Rodman, C., Luo, C.L., Mroz, E.A., Emerick, K.S., et al. (2017). Single-cell transcriptomic analysis of primary and metastatic tumor ecosystems in head and neck cancer. Cell *171*, 1611–1624.e24.

18. Tirosh, I., Izar, B., Prakadan, S.M., Wadsworth, M.H., 2nd, Treacy, D., Trombetta, J.J., Rotem, A., Rodman, C., Lian, C., Murphy, G., et al. (2016). Dissecting the multicellular ecosystem of metastatic melanoma by single-cell RNA-seq. Science *352*, 189–196.

19. Liu, S., Liang, J., Liu, Z., Zhang, C., Wang, Y., Watson, A.H., Zhou, C., Zhang, F., Wu, K., Zhang, F., et al. (2021). The Role of CD276 in Cancers. Front. Oncol. *11*, 654684.

20. Turula, H., and Wobus, C.E. (2018). The role of the polymeric immunoglobulin receptor and secretory immunoglobulins during mucosal infection and immunity. Viruses *10*, 237.

21. Beswick, E.J., and Reyes, V.E. (2009). CD74 in antigen presentation, inflammation, and cancers of the gastrointestinal tract. World J. Gastroenterol. *15*, 2855–2861.

22. Lee, J.W., Stone, M.L., Porrett, P.M., Thomas, S.K., Komar, C.A., Li, J.H., Delman, D., Graham, K., Gladney, W.L., Hua, X., et al. (2019). Hepatocytes direct the formation of a pro-metastatic niche in the liver. Nature *567*, 249–252.

23. Lozupone, C., Lladser, M.E., Knights, D., Stombaugh, J., and Knight, R. (2011). UniFrac: an effective distance metric for microbial community comparison. ISME J. *5*, 169–172.

24. McMurdie, P.J., and Holmes, S. (2013). phyloseq: An R Package for Reproducible Interactive Analysis and Graphics of Microbiome Census Data. PLoS One *8*, e61217.

25. Meyer, M.A., Baer, J.M., Knolhoff, B.L., Nywening, T.M., Panni, R.Z., Su, X., Weilbaecher, K.N., Hawkins, W.G., Ma, C., Fields, R.C., et al. (2018). Breast and pancreatic cancer interrupt IRF8-dependent dendritic cell development to overcome immune surveillance. Nat. Commun. *9*, 1250.

26. Bayne, L.J., Beatty, G.L., Jhala, N., Clark, C.E., Rhim, A.D., Stanger, B.Z., and Vonderheide, R.H. (2012). Tumor-derived granulocyte-macrophage colony-stimulating factor regulates myeloid inflammation and t cell immunity in pancreatic cancer. Cancer Cell *21*, 822–835.

27. Markosyan, N., Li, J., Sun, Y.H., Richman, L.P., Lin, J.H., Yan, F., Quinones, L., Sela, Y., Yamazoe, T., Gordon, N., et al. (2019). Tumor cell-intrinsic EPHA2 suppresses anti-tumor immunity by regulating PTGS2 (COX-2). J. Clin. Invest. *129*, 3594–3609.

28. Li, J., Yuan, S., Norgard, R.J., Yan, F., Yamazoe, T., Blanco, A., and Stanger, B.Z. (2020). Tumor Cell–Intrinsic USP22 Suppresses Antitumor Immunity in Pancreatic Cancer. Cancer Immunol. Res. *8*, 282–291.

29. Spranger, S., Bao, R., and Gajewski, T.F. (2015). Melanoma-intrinsic β-catenin signalling prevents anti-tumour immunity. Nature 523, 231–235.

30. Baruch, E.N., Youngster, I., Ben-Betzalel, G., Ortenberg, R., Lahat, A., Katz, L., Adler, K., Dick-Necula, D., Raskin, S., Bloch, N., et al. (2021). Fecal microbiota transplant promotes response in immunotherapy-refractory melanoma patients. Science 371, 602–609.

31. Davar, D., Dzutsev, A.K., McCulloch, J.A., Rodrigues, R.R., Chauvin, J.M., Morrison, R.M., Deblasio, R.N., Menna, C., Ding, Q., Pagliano, O., et al. (2021). Fecal microbiota transplant overcomes resistance to anti–PD-1 therapy in melanoma patients. Science 371, 595–602.

32. Gopalakrishnan, V., Spencer, C.N., Nezi, L., Reuben, A., Andrews, M.C., Karpinets, T.V., Prieto, P.A., Vicente, D., Hoffman, K., Wei, S.C., et al. (2018). Gut microbiome modulates response to anti-PD-1 immunotherapy in melanoma patients. Science 359, 97–103.

33. Routy, B., Le Chatelier, E., Derosa, L., Duong, C.P.M., Alou, M.T., Daillère, R., Fluckiger, A., Messaoudene, M., Rauber, C., Roberti, M.P., et al. (2018). Gut microbiome influences efficacy of PD-1–based immunotherapy against epithelial tumors. Science 359, 91–97.

34. Sivan, A., Corrales, L., Hubert, N., Williams, J.B., Aquino-Michaels, K., Earley, Z.M., Benyamin, F.W., Lei, Y.M., Jabri, B., Alegre, M.L., et al. (2015). Commensal Bifidobacterium promotes antitumor immunity and facilitates anti–PD-L1 efficacy. Science 350, 1084–1089.

35. Vétizou, M., Pitt, J.M., Daillère, R., Lepage, P., Waldschmitt, N., Flament, C., Rusakiewicz, S., Routy, B., Roberti, M.P., Duong, C.P.M., et al. (2015). Anticancer immunotherapy by CTLA-4 blockade relies on the gut microbiota. Science 350, 1079–1084.

36. Beatty, G.L., Werba, G., Lyssiotis, C.A., and Simeone, D.M. (2021). The biological underpinnings of therapeutic resistance in pancreatic cancer. Genes Dev. 35, 940–962.

37. van der Zande, H.J.P., Nitsche, D., Schlautmann, L., Guigas, B., and Burgdorf, S. (2021). The Mannose Receptor: From Endocytic Receptor and Biomarker to Regulator of (Meta)Inflammation. Front. Immunol. 12, 765034.

38. Galeano Niño, J.L., Wu, H., LaCourse, K.D., Kempchinsky, A.G., Baryiames, A., Barber, B., Futran, N., Houlton, J., Sather, C., Sicinska, E., et al. (2022). Effect of the intratumoral microbiota on spatial and cellular heterogeneity in cancer. Nature 611, 810–817.

39. Ghaddar, B., Biswas, A., Harris, C., Omary, M.B., Carpizo, D.R., Blaser, M.J., and De, S. (2022). Tumor microbiome links cellular programs and immunity in pancreatic cancer. Cancer Cell 40, 1240–1253.e5.

40. Alam, A., Levanduski, E., Denz, P., Villavicencio, H.S., Bhatta, M., Alhorebi, L., Zhang, Y., Gomez, E.C., Morreale, B., Senchanthisai, S., et al. (2022). Fungal mycobiome drives IL-33 secretion and type 2 immunity in pancreatic cancer. Cancer Cell 40, 153–167.e11.

41. Mi, H., Muruganujan, A., Ebert, D., Huang, X., and Thomas, P.D. (2019). PANTHER version 14: more genomes, a new PANTHER GO-slim and improvements in enrichment analysis tools. Nucleic Acids Res. 47, D419–D426.

42. Bindea, G., Mlecnik, B., Hackl, H., Charoentong, P., Tosolini, M., Kirilovsky, A., Fridman, W.H., Pagès, F., Trajanoski, Z., and Galon, J. (2009). ClueGO: a Cytoscape plug-in to decipher functionally grouped gene ontology and pathway annotation networks. Bioinformatics 25, 1091–1093.

43. Shannon, P., Markiel, A., Ozier, O., Baliga, N.S., Wang, J.T., Ramage, D., Amin, N., Schwikowski, B., and Ideker, T. (2003). Cytoscape: a software environment for integrated models of biomolecular interaction networks. Genome Res. 13, 2498–2504.

44. Subramanian, A., Tamayo, P., Mootha, V.K., Mukherjee, S., Ebert, B.L., Gillette, M.A., Paulovich, A., Pomeroy, S.L., Golub, T.R., Lander, E.S., and Mesirov, J.P. (2005). Gene set enrichment analysis: a knowledge-based approach for interpreting genome-wide expression profiles. Proc. Natl. Acad. Sci. USA 102, 15545–15550.

45. Carpenter, A.E., Jones, T.R., Lamprecht, M.R., Clarke, C., Kang, I.H., Friman, O., Guertin, D.A., Chang, J.H., Lindquist, R.A., Moffat, J., et al. (2006). CellProfiler: image analysis software for identifying and quantifying cell phenotypes. Genome Biol. 7, R100.

46. Berg, S., Kutra, D., Kroeger, T., Straehle, C.N., Kausler, B.X., Haubold, C., Schiegg, M., Ales, J., Beier, T., Rudy, M., et al. (2019). ilastik: interactive machine learning for (bio)image analysis. Nat. Methods 16, 1226–1232.

47. Schapiro, D., Jackson, H.W., Raghuraman, S., Fischer, J.R., Zanotelli, V.R.T., Schulz, D., Giesen, C., Catena, R., Varga, Z., and Bodenmiller, B. (2017). histoCAT: analysis of cell phenotypes and interactions in multiplex image cytometry data. Nat. Methods 14, 873–876.

48. Love, M.I., Huber, W., and Anders, S. (2014). Moderated estimation of fold change and dispersion for RNA-seq data with DESeq2. Genome Biol. 15, 550.

49. Bhuva, D.D., Cursons, J., and Davis, M.J. (2020). Stable gene expression for normalisation and single-sample scoring. Nucleic Acids Res. 48, e113.

50. Rooney, M.S., Shukla, S.A., Wu, C.J., Getz, G., and Hacohen, N. (2015). Molecular and genetic properties of tumors associated with local immune cytolytic activity. Cell 160, 48–61.

51. Ho, W.J., Zhu, Q., Durham, J., Popovic, A., Xavier, S., Leatherman, J., Mohan, A., Mo, G., Zhang, S., Gross, N., et al. (2021). Neoadjuvant cabozantinib and nivolumab convert locally advanced hepatocellular carcinoma into resectable disease with enhanced antitumor immunity. Nat. Cancer 2, 891–903.

52. Zabransky, D.J., Danilova, L., Leatherman, J.M., Lopez-Vidal, T.Y., Sanchez, J., Charmsaz, S., Gross, N.E., Shin, S., Yuan, X., Hernandez, A., et al. (2023). Profiling of syngeneic mouse HCC tumor models as a framework to understand anti–PD-1 sensitive tumor microenvironments. Hepatology 77, 1566–1579.

53. Van Gassen, S., Callebaut, B., Van Helden, M.J., Lambrecht, B.N., Demeester, P., Dhaene, T., and Saeys, Y. (2015). FlowSOM: Using self-organizing maps for visualization and interpretation of cytometry data. Cytometry A. 87, 636–645.

STAR★METHODS

KEY RESOURCES TABLE

REAGENT or RESOURCE	SOURCE	IDENTIFIER
Antibodies		
Rat monoclonal anti-mouse CD3 (17A2)	BioLegend	100214; RRID:AB_493644
Rat monoclonal anti-mouse CD4 (RM4-5)	Invitrogen	17-0042-82; RRID:AB_469323
Rat monoclonal anti-mouse CD8 (53-6.7)	BioLegend	100708; RRID:AB_312747
Rat monoclonal anti-mouse CD11b (M1/70)	BD Biosciences	550993; RRID:AB_394002
Rat monoclonal anti-mouse CD45 (30-F11)	BioLegend	103125; RRID:AB_493536
Rat monoclonal anti-mouse CD45 (30-F11)	BD Biosciences	550994; RRID:AB_394003
Rat monoclonal anti-mouse CD45 (30-F11)	BD Biosciences	442848
Rat monoclonal anti-mouse CD74 (In1/CD74)	BioLegend	151004; RRID:AB_2632609
Rat monoclonal anti-mouse CD86 (GL1)	BD Biosciences	553692; RRID:AB_394994
Rat monoclonal anti-mouse CD206 (MR6F3)	eBioscience	17-2061-82; RRID:AB_2637420
Rat monoclonal anti-mouse E-cadherin (DECMA-1)	BioLegend	47314; RRID:AB_2750302
Rat monoclonal anti-mouse F4/80 (BM8)	BioLegend	123114; RRID:AB_893478
Rat monoclonal anti-mouse F4/80 (BM8)	BioLegend	123118; RRID:AB_893489
Rat monoclonal anti-mouse Ly6G (1A8)	BD Biosciences	560602; RRID:AB_1727563
Rat monoclonal anti-mouse MHC class I (28-8-6)	BioLegend	114608; RRID:AB_313599
Rat monoclonal anti-mouse MHC class I (M5/114.15.2)	BioLegend	107627; RRID:AB_1659252
Rat monoclonal anti-mouse PD-L1 (10F.9G2)	BioLegend	124314; RRID:AB_10643573
Rat monoclonal anti-mouse CD4 (GK1.4)	BioXcell	BE0003-1; RRID:AB_1107636
Rat monoclonal anti-mouse CD8 (2.42)	BioXcell	BE0061; RRID:AB_1125541
Mouse monoclonal anti-human CD1a (O10)	Thermo Fisher	MA5-12526; RRID:AB_10943672
Rabbit monoclonal anti-human CD3 (2GV6)	Ventana	790-4341; RRID:AB_2335978
Rabbit monoclonal anti-human CD8 (SP57)	Ventana	760-4460;RRID:AB_2335985
Rabbit monoclonal anti-mouse CD8 (EPR20305)	Abcam	ab209775; RRID:AB_2860566
Mouse monoclonal anti-human CD15 (MMA)	Ventana	760-2504; RRID:AB_2335952
Rabbit monoclonal anti-mouse CD19 (D4V4B)	Cell Signaling Technology	90176S; RRID:AB_2800152
Mouse monoclonal anti-human CD20 (L26)	Ventana	760-2531; RRID:AB_2335956
Mouse monoclonal anti-human CD31 (JC70)	Cell Marque	760-4378; RRID:AB_2927455
Rabbit monoclonal anti-mouse CD31 (D8B9E)	Cell Signaling Technology	77699; RRID:AB_2722705
Mouse monoclonal anti-human CD68 (KP-1)	Ventana	790-2931; RRID:AB_2335972
Mouse monoclonal anti-human CD74 (LN2)	Abcam	ab9514; RRID:AB_2075504
Rabbit monoclonal anti-human CD276 (SP206)	Abcam	ab227670
Rabbit monoclonal anti-human citrullinated histone H3 (E4O3F)	Cell Signaling Technology	97272S
Mouse monoclonal anti-human CK19 (A53-B/A2.26)	Ventana	760-4281; RRID:AB_2335655
Rabbit monoclonal anti-rabbit CK19 (EPNCIR127B)	Abcam	ab133496; RRID:AB_11155282
Mouse monoclonal anti-human FOXP3 (236A/E7)	Abcam	ab20034; RRID:AB_445284
Rabbit monoclonal anti-mouse FOXP3 (D6O8R)	Cell Signaling Technology	12653; RRID:AB_2797979
Mouse monoclonal anti-human HLA-ABC (EMR8-5)	Abcam	ab70328; RRID:AB_1269092
Rabbit monoclonal anti-human IgA (EPR5367-76)	Abcam	ab124716; RRID:AB_10976507
Rabbit monoclonal anti-human IgG (EPR4421)	Abcam	ab109489;RRID:AB_10863040
Rabbit monoclonal anti-human Ki-67 (30-9)	Ventana	790-4286;RRID:AB_2631262
Mouse monoclonal anti-LPS (2D7/1)	Abcam	ab35654;RRID:AB_732222
Mouse polyclonal anti-LTA	Hycult Biotech	HM2048;RRID:AB_57466

(Continued on next page)

Continued

REAGENT or RESOURCE	SOURCE	IDENTIFIER
Mouse monoclonal anti-human PD-1 (NAT105)	Abcam	ab52587;RRID:AB_881954
Rabbit monoclonal anti-human PD-L1 (SP263)	Ventana	740-4907;RRID:AB_2819099
Rabbit polyclonal anti-human PIGR	Novus Biologicals	NBP1-86095; RRID:AB_11012087
Mouse monoclonal anti-human podoplanin (D2-40)	Ventana	760-4395
Rabbit monoclonal anti-human TIM3 (D5D5R)	Cell Signaling Technology	45208; RRID:AB_2716862
Rabbit polyclonal anti-human TOX	Invitrogen	PA5-53781; RRID:AB_2648830
Mouse monoclonal anti-mouse αSMA (1A4)	Cell Signaling Technology	69319SF
Rabbit monoclonal anti-mouse vimentin (D21H3)	Cell Signaling Technology	46173SF
Rabbit monoclonal anti-mouse S100A9 (D3U8M)	Cell Signaling Technology	74641SF
Hamster monoclonal anti-mouse podoplanin (8.1.1)	BioLegend	127401; RRID:AB_108918
Rabbit monoclonal anti-mouse CD11c (D1V9Y)	Cell Signaling Technology	39143SF; RRID:AB_2924836
Rabbit monoclonal anti-mouse CD68 (E3O7V)	Cell Signaling Technology	29176SF
Rat monoclonal anti-mouse MHC class II (M5/114.15.2)	Thermo Fisher	14-5321-82; RRID:AB_467561
Rabbit monoclonal anti-mouse CD206 (E6T5J)	Cell Signaling Technology	87887SF
Rabbit monoclonal anti-mouse CD10 (EPR22867-118)	Abcam	ab261729
Mouse monoclonal anti-mouse Ki-67 (B56)	Standard BioTools	91H017150
Rabbit monoclonal anti-mouse CD45 (D3F8Q)	Standard BioTools	91H029151
Rabbit monoclonal anti-mouse CD31 (D8V9E)	Cell Signaling Technology	92841SF; RRID:AB_2940919
Rabbit monoclonal anti-mouse TOX/TOX2 (E6I3Q)	Cell Signaling Technology	62886SF
Rabbit monoclonal anti-mouse PD-1 (EPR20665)	Abcam	ab228857
Rabbit monoclonal anti-mouse GZMB (EPR22645-206)	Standard BioTools	91H026155
Rabbit monoclonal anti-mouse F4/80 (D2S9R)	Standard BioTools	91H030156
Rabbit monoclonal anti-mouse E-cadherin (24E10)	Standard BioTools	3158029D; RRID:AB_2893074
Rabbit monoclonal anti-mouse CD3 (E4T1B)	Cell Signaling Technology	73484SF
Rabbit monoclonal anti-mouse CD8 (EPR21769)	Standard BioTools	91H023162
Rabbit monoclonal anti-mouse CD11b (EPR1344)	Standard BioTools	91H007163
Mouse monoclonal anti-mouse NK1.1 (PK136)	Thermo Fisher	MA1-70100; RRID:AB_2296673
Rat monoclonal anti-mouse FOXP3 (FJK-16s)	Standard BioTools	91H032165
Rat monoclonal anti-mouse Ly6G (1A8)	Standard BioTools	91H037166
Rabbit monoclonal anti-mouse CD86 (E5W6H)	Cell Signaling Technology	20018SF
Rabbit monoclonal anti-mouse PD-L1 (D5V3B)	Cell Signaling Technology	85095SF
Rat monoclonal anti-mouse B220 (RA3-6B2)	Standard BioTools	91H036176
Biological samples		
Human: FFPE tumor blocks	Cooperative Human Tissue Network	https://www.chtn.org
Chemicals, peptides, and recombinant proteins		
Human *CCL19* probe	ACDBio	474369
Human *CD276* probe	ACDBio	430419
Deposited data		
Sequencing data	This paper	GEO: GSE155725
Sequencing data	This paper	GEO: GSE213736
Experimental models: Cell lines		
Mouse: 69	Lee et al.[22]	N/A
Mouse: 6419c5	Li et al.[16]	N/A
Mouse: 6422c1	Li et al.[16]	N/A
Mouse: 6694c2	Li et al.[16]	N/A
Mouse: 2838c3	Li et al.[16]	N/A
Mouse: 6499c4	Li et al.[16]	N/A
Mouse: 6620c1	Li et al.[16]	N/A

Continued

REAGENT or RESOURCE	SOURCE	IDENTIFIER
Oligonucleotides		
Universal 16S primers targeting v4 region: 515F, 5'-GTGYCAGCMGCCGCGGTAA-3'; 806R, 5'- GGACTACNVGGGTWTCTAAT-3'	This paper	N/A
Experimental models: Organisms/strains		
Mouse: C57BL/6J	The Jackson Laboratory	JAX: 000664
Software and algorithms		
Visiopharm Integrator System (VIS) software	Visiopharm	https://visiopharm.com
PANTHER	Mi et al.[41]	https://pantherdb.org
ClueGO	Bindea et al.[42]	https://apps.cytoscape.org/apps/cluego
Cytoscape	Shannon et al.[43]	https://cytoscape.org
GSEA	Subramanian et al.[44]	https://www.gsea-msigdb.org
CellProfiler	Carpenter et al.[45]	https://cellprofiler.org
Ilastik	Berg et al.[46]	https://www.ilastik.org
HistoCAT	Schapiro et al.[47]	https://bodenmillergroup.github.io/histocat-web

RESOURCE AVAILABILITY

Lead contact

Further information and requests for resources and reagents should be directed to and will be fulfilled by the lead contact, Gregory L. Beatty (gregory.beatty@pennmedicine.upenn.edu).

Materials availability

This study did not generate new unique reagents.

Data and code availability

- Sequencing data have been deposited at GEO and are publicly available as of the date of publication. Accession numbers are listed in the key resources table. All data reported in this paper will be shared by the lead contacts upon request.
- This paper does not report original code.
- Any additional information required to reanalyze the data reported in this paper is available from the lead contacts upon request.

EXPERIMENTAL MODEL AND STUDY PARTICIPANT DETAILS

Human samples

Deidentified formalin-fixed paraffin-embedded (FFPE) patient tumor samples were acquired from the Cooperative Human Tissue Network. Written informed consent was obtained prior to the procurement of all patient specimens. Tissue collection protocols were approved by the institutional review board of the University of Pennsylvania and were carried out in compliance with the 1996 Declaration of Helsinki. Patient characteristics are shown in Table S2.

Cell lines

"Cold" PDAC cell lines (69, 6419c5, 6422c1, and 6694c2) and "hot" PDAC cell lines (2838c3, 6499c4, and 6620c1) were used for orthotopic injection. These cell lines were derived from PDAC tumors that arose spontaneously in $Kras^{LSL-G12D/+}$ $Trp53^{LSL-R172H/+}$ $Pdx1-cre$ (KPC) mice, as previously described.[16,22] Cell lines were cultured in DMEM (Corning) supplemented with 10% fetal bovine serum (FBS, VWR), 83 μg/ml gentamicin (Thermo Fisher), and 1% GlutaMAX (Thermo Fisher) at 37°C, 5% CO2. Trypan blue staining was used to ensure that cells with >95% viability were used for studies. Cell lines were tested routinely for *Mycoplasma* contamination at the Cell Center Services Facility at the University of Pennsylvania. All cell lines used in our studies tested negative for *Mycoplasma* contamination.

In vivo studies

Female C57BL/6J mice of similar age were obtained from the Jackson Laboratory. Sample sizes were estimated based on pilot experiments. Animal protocols were reviewed and approved by the Institute of Animal Care and Use Committee of the University of Pennsylvania. Mice were monitored three times per week for general health and euthanized early based on defined endpoint criteria

including significant ascites, lethargy, loss of $\geq 10\%$ body weight, or other signs of sickness or distress. A cocktail of antibiotics, including metronidazole (20 mg/kg, Sigma), ceftriaxone (50 mg/kg, Sigma), and vancomycin (20 mg/kg, Sigma), was administered twice daily via intraperitoneal injection beginning on day -3 until day 20. Anti-CD4 (clone GK1.5, 0.2 mg, BioXCell) and anti-CD8 (clone 2.43, 0.2 mg, BioXCell) antibodies were administered on days -3, 4, 11 and 18. Mice were orthotopically injected with tumor cells (5 × 10^5 cells suspended in 100 μL sterile PBS) into the pancreas on day 0, as previously described.[22]

METHOD DETAILS

Microscopic analysis

FFPE tissue blocks containing human primary tumors were sectioned at 5 μm onto Superfrost Plus microscope slides (VWR International, catalog 48311-703). Automated immunohistochemistry, immunofluorescence, and RNA *in situ* hybridization were performed using a Ventana Discovery Ultra automated slide staining system (Roche). Reagents used for deparaffinization, heat-induced epitope retrieval, and chromogenic or fluorescent signal detection were obtained from Roche and ACDBio and used according to the manufacturer's protocol. All antibodies and reagents used for microscopic analysis are shown in Table S3. Images were acquired using a BX43 upright microscope (Olympus), an Aperio CS2 scanner system (Leica), and an IX83 inverted multicolor fluorescent microscope (Olympus).

Immunohistochemistry image analysis

Whole slide scanned images were digitally quantified using Visiopharm Integrator System (VIS) software (Version 2019.07). For immune cell heterogeneity analyses, 250 μm by 250 μm square grids were superimposed upon stained tissues. Regions containing adipose tissue, necrotic lesions, and artefactual staining were excluded from analysis. Cell identity was then quantified as the number of cells within each grid. Cell counts were normalized to the area of the grid and reported as densities (cells per mm^2). Spatial variance in $CD8^+$ T cell density was calculated across constituent grids making up a single patient tissue sample. Spatial variance was defined as the square of the standard deviation. $CD8^+$ T cell spatial heterogeneity was visualized using heat maps based on the number of $CD8^+$ T cells detected within each square grid. The same minimum and maximum thresholds were applied to all samples during heat map generation. For virtual biopsy analyses, rectangular grids measuring 20 μm by 3,000 μm were superimposed on whole slide scans of pancreatic tumor tissues. Each grid was designed to simulate tissue captured in a core needle biopsy. Images were quantified, and the density of $CD8^+$ and $FOXP3^+$ T cells was reported for each virtual biopsy grid.

T cell-enriched ("hot") and -poor ("cold") tumor nests were detected computationally using heat maps in an unsupervised manner. We defined a tumor nest as a localized region consisting of a cluster of cancer cells and the immediate stroma surrounding the cancer cells. To identify these focal regions, cancer cells and their surrounding immune infiltrates were classified in an unsupervised manner using the VIS software. We generated heat maps based on the CD8 density in classified images. To normalize the margins of the tumor nests, a uniform distance of 150 μm from $CK19^+$ cancer cells was applied during CD8 heatmap generation. Results from heat-map generation were used to guide subsequent manual delineation of regions of interest (ROIs) around (i) tumor nests with low CD8 density and (ii) tumor nests with high CD8 density. Finally, tumor nests, excluding ductal lumens, with >500 $CD8^+$ T cells per mm^2 were designated as hot tumor nests, and regions that did not meet this threshold were designated as cold tumor nests.

For epithelial-based analyses, only $CK19^+$ tumor cells were examined. For stromal-based analyses, $CK19^+$ tumor cells were excluded from tumor nests. The absolute number of cells expressing markers of interest was quantified using the VIS software, normalized to the area of the ROI, and reported as densities (number of cells per mm^2). Furthermore, percent area of positive staining was determined within the ROI.

Immunofluorescence image analysis

Spatial distribution of gram-negative bacteria in solid tumors was assessed using whole slide images of human pancreatic ductal adenocarcinoma and lung adenocarcinoma specimens acquired on a Leica Aperio FL ScanScope Pathology Slide Scanner. ROIs were delineated around nucleated (i.e., DAPI-positive) regions. Lipopolysaccharide (LPS)-positive staining was quantified using the VIS software. Heat maps based on LPS signal were generated to visualize the distribution of gram-negative bacteria. To quantify differences in LPS distribution patterns, square grids measuring 250 μm by 250 μm were superimposed upon tissues. Percent area of LPS positive staining was assessed per grid. Spatial variance in LPS percent area was calculated across constituent grids making up a single patient tissue sample and within epithelial and stromal regions. Cell-enriched and -poor tumor nests were defined based on k-means clustering, and percent LPS-positive staining quantified using the VIS software. In addition, the VIS "Multiplex Phenotyping" platform was used to detect T cell phenotypes. The sum of all absolute cell counts was used to calculate percent composition of each T cell phenotype in cold and hot tumor nests. For analysis of the spatial distribution of LPS and 16S rRNA, at least five 20× fields were captured from each tumor specimen. Co-localization of LPS and 16S rRNA with cells expressing markers of interest were then examined using Olympus cellSens software.

RNA and laser capture microdissection (LCM)

For isolation of RNA from whole slides (Figure S4A), FFPE tissues were sectioned onto Superfrost Plus microscope slides and macrodissected. RNA was isolated using a RNeasy FFPE kit (Qiagen, catalog 73504) following the manufacturer's protocol. For isolation of

RNA from mouse tumors (Figures 4A and S11A), a RNeasy Mini kit (Qiagen, catalog 74004) was used following the manufacturer's protocol. For isolation of RNA from tumor nests (Figures 2E and S5A), FFPE blocks containing human primary tumors were serially sectioned at 5 μm onto glass slides with PEN membrane (Leica, catalog 11505158), air dried, and stored at -80°C until analysis. Slides were then thawed at room temperature prior to use and deparaffinized in fresh xylene for 30 seconds twice, followed by rehydration in ethanol (30 seconds each in 100%, 100%, 95%, and 70% ethanol). Slides were transferred to RNase-free water and stained with Mayer's hematoxylin for 10 seconds. Slides were washed with RNase-free water and dehydrated in 95% ethanol, 100% ethanol, and xylene, twice in each solution for 30 seconds. Specific regions of dehydrated slides were micro-dissected by laser capture using a LMD7000 microscope (Leica). For isolation of tumor epithelium and stroma (Figure S5A), tumor epithelium and adjacent stroma were identified using the morphology of cells that were stained with hematoxylin as described above, and specific regions were then isolated using LCM. For isolation of tumor epithelium and stroma from cold and hot tumor nests (Figure 2E), regions that corresponded to cold and hot tumor nests were determined using a serial section that was stained with CK19, CD68, FOXP3, CD8, and hematoxylin using immunohistochemistry as described above. Tumor epithelium and adjacent stroma from cold and hot tumor nests were then isolated using LCM. RNA from stroma and epithelium was isolated using a RNeasy FFPE kit, and RNA from cold and hot stroma and epithelium was collected using a NucleoSpin total RNA FFPE XS kit (Takara, catalog 740969.50). The quality of all RNA samples was assessed using a 2100 Bioanalyzer (Agilent).

RNA sequencing and data analysis

The quality of RNA isolated from human or mouse pancreatic tumors was determined using a 2100 Bioanalyzer (Agilent). Samples were then prepared using a QuantSeq 3′ mRNA-Seq library prep kit FWD for Illumina (Lexogen) or SMARTer stranded total RNA-Seq kit v2 (Takara) following the manufacturer's protocol and analyzed on a NextSeq 500 sequencing system (Illumina) at the Genomics Facility at the Wistar Institute. FASTQ files were uploaded to the BaseSpace Suite (Illumina), and the quality of FASTQ files was assessed using FastQC application (version 1.0.0). All FASTQ files used in this study passed per base sequence quality checks with most bases having per sequence quality scores higher than 30. FASTQ files were aligned using BaseSpace Suite RNA-Seq Alignment application (version 2.0.0) (Data S1). Output files were analyzed using RNA-Seq Differential Expression application (version 1.0.1). DEGs were determined using DESeq2,[48] PANTHER,[41] and ClueGO (version 2.5.6),[42] an application of Cytoscape software (version 3.7.2).[43] For ClueGO analysis, functional grouping of biological processes was performed based on kappa score, and only pathways with P values less than 0.05 were visualized. Gene set enrichment analysis (GSEA, version 3.0)[44] and *singscore* in R[49] were used to determine biological processes that were enriched in cold and hot tumor nests. Cytolytic activity in tumor nests was calculated as the geometric mean of *GZMA* and *PRF1*, as previously described.[50] Volcano plots were generated using Prism (GraphPad Software, version 9), and heat maps were plotted using *pheatmap* in R (version 4.2).

Flow cytometry

Tumors were minced and incubated in 37°C for 45 min in DMEM containing collagenase (1 mg/mL, Sigma-Aldrich) and DNase (150 U/mL, Roche). Tissues were then filtered through a 70-μm cell strainer, washed with DMEM, and lysed using ACK lysing buffer (Life Technologies). Cells were washed, stained with antibodies (Table S3), and acquired on a FACS Canto II (BD Biosciences). FlowJo software (Treestar) was used to analyze flow cytometric data.

16S rRNA gene quantification

Total bacterial genomic DNA was extracted from FFPE sections containing human PDAC tissues, frozen mouse tumors, and mouse stool samples using a QIAamp DNA FFPE Tissue Kit, QIAamp DNA Mini Kit, and QIAamp PowerFecal Pro DNA Kit (Qiagen), respectively, following the manufacturers' instructions. DNA concentration was measured using a Qubit 4 Fluorometer (Thermo Scientific) and kept at -80°C until analysis. For 16S rRNA gene quantitative PCR, universal 16S primers targeting the v4 region (515F, 5′-GTGYC AGCMGCCGCGGTAA-3′ and 806R, 5′- GGACTACNVGGGTWTCTAAT-3′) were used. Sterile water was used as a negative control. Equal amounts of genomic DNA (100 ng) were used for each tumor or stool sample. Relative 16S rRNA levels were calculated by normalizing C*t* values of the samples to the median C*t* value of cold tumors or stools collected from mice bearing cold tumors. Additionally, we utilized *Escherichia coli* genomic DNA at various concentrations ranging from 0 to 1,000,000 ng/μL to generate a standard curve. This standard curve was then used to calculate the absolute amount of 16S rRNA that was present in each sample (Figure S15).

16S rRNA metagenomic sequencing and analysis

Following extraction of total bacterial genomic DNA, the v3-v4 region of the 16S rRNA gene was amplified with gene specific primers (314F and 806R) added with overhang adapters using a 16S V3-V4 Library Preparation Kit (Illumina). The amplicon library was sequenced on a MiSeq platform (Illumina) using a 2 × 250 bp paired-end protocol. QIIME 2 pipeline was then used to analyze the 16S sequencing data. Specifically, Casava 1.8 paired-end demultiplexed FASTQ data was imported into QIIME 2, followed by quality filtering, length trimming, and denoise with Deblur. Sequences were then clustered into Operational Taxonomic Units (OTUs) at 97% identity, and the chimera were filtered using *q2-vsearch*. Taxonomy assigned with the Greengenes 13_8 database was analyzed using *q2-feature-classifier*. OTUs less than 3 and sequence counts less than 10 were excluded from analysis. Phylogenetic trees were

generated using *q2-phylogeny*. Alpha diversity (Faith-PD, observed features, and Shannon index) and beta diversity (Bray-Curtis, Jaccard, and unweighted UniFrac distance metrics) analyses were performed using *q2-diversity*.

Image mass cytometry (IMC)

IMC staining on mouse liver tissues were performed as previously described.[51,52] FFPE sections were baked, deparaffinized in xylene, then rehydrated in an alcohol gradient. Slides were incubated in Cell Condition Solution 1 (Roche) at 100°C for 1 hour then blocked with 3% BSA for 45 min at room temperature, followed by overnight staining at 4°C with the antibody cocktail. Antibodies, metal isotopes, and their titrations are listed in Table S4. Images were acquired using a Hyperion Image System (Standard BioTools). From each section, images were obtained from 6 ROIs, each measuring at least 1 mm by 1 mm. Upon acquisition, representative images were visualized and generated through MCD Viewer (Standard BioTools). For data analysis, images were segmented into a single cell dataset using the publicly available software pipeline based on CellProfiler, ilastik, and HistoCAT.[45–47] The resulting single cells were clustered using all mouse cell markers using FlowSOM[53] into metaclusters, which were annotated into final cell types, as previously described.[51,52] Cell type density quantifications were performed by calculating the number of cells of each cell type over the area of each ROI.

Correlation analysis

Relative 16S rRNA levels in tumor and stool, total numbers of cells and percentages of cells positive for surface molecules and tumor weights were imported into R studio (R version 4.2) and used for analyses following normalization. PCA plot, heat map, and correlation matrix were generated using *ggplot*, *pheatmap*, and *corrplot* R packages, respectively.

QUANTIFICATION AND STATISTICAL ANALYSIS

Statistical significance was calculated using Prism (GraphPad Software, version 9) unless indicated otherwise. Multiple comparisons testing was performed using one-way ANOVA with Dunnett's test to compare the statistical difference between the control group to all other experimental groups or Kruskal-Wallis test. Unpaired group comparisons test was performed using two-tailed Mann-Whitney test. Correlation analysis was performed using Pearson's correlation. *P* values less than 0.05 were treated as significant. The investigators were not blinded to allocation during experiments and outcome assessment.